

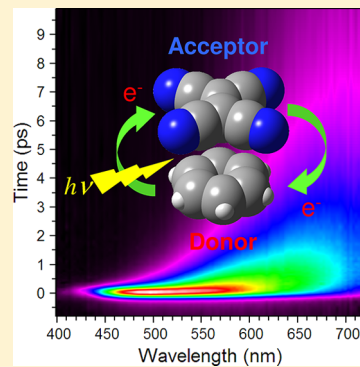
Ultrafast Time-Resolved Broadband Fluorescence Studies of the Benzene-Tetracyanoethylene Complex: Solvation, Vibrational Relaxation, and Charge Recombination Dynamics

Chih-Chung Chiu, Chih-Chang Hung, Chien-Lin Chen, and Po-Yuan Cheng*

Department of Chemistry, National Tsing Hua University, Hsinchu, Taiwan 30043, Republic of China

Supporting Information

ABSTRACT: The charge-transfer (CT) state relaxation dynamics of the benzene-tetracyanoethylene (BZ–TCNE) complex was studied with broadband ultrafast time-resolved fluorescence spectroscopy implemented by optical Kerr gating in three solvents of different polarities. The CT state of the BZ–TCNE complex is reached via femtosecond laser excitation, and the subsequent temporal evolutions of the fluorescence spectra were measured. Analyses of various time-dependent spectral properties revealed rapid relaxations along solvent and vibrational coordinates in competition with charge recombination (CR). By comparing the results in solvents of different polarities, we partially separated solvation and vibrational relaxation dynamics and explored the solvent-dependent CR dynamics. Time-dependent dynamic fluorescence Stokes shift (TDFSS) measurements unveiled the solvation and vibrational relaxation contributions to the observed spectral relaxation. The biphasic and slow time scales of the vibrational contributions identified in TDFSS suggested nonstatistical and hindered intramolecular vibrational-energy redistribution that can be attributed to the unique structural properties of EDA complexes. The slowest spectral relaxation of 10–15 ps identified in TDFSS was ascribed to relaxation of the $\text{BZ}^+–\text{TCNE}^-$ intermolecular vibrations, which is equivalent to a structural relaxation from the initial Franck–Condon configuration to the equilibrium CT-state structure. The time scales of vibrational relaxation indicate that a fraction of the CT-state population undergoes CR reactions before complete vibrational/structural equilibrium is achieved. In carbon tetrachloride, a nonexponential temporal profile was observed and attributed to vibrational nonequilibrium CR. In dichloromethane, polar solvation greatly accelerates CR reactions, and a slower reaction-field-induced structural relaxation gives rise to a pronounced biexponential decay. The equilibrium CR time constants of the BZ–TCNE CT state are 29 ps, 150 ps, and 68 ps in dichloromethane, carbon tetrachloride, and cyclohexane, respectively.



1. INTRODUCTION

Charge separation (CS) initiated by photoexcitation is the most essential initial step in photosynthesis as well as in many artificial systems that convert light into other forms of energy, whereas the charge recombination (CR) following CS is usually the undesired energy-wasting process.¹ The dye-sensitized solar cell is a good example of recent interests in which the photoinduced CS and the subsequent CR play important roles regarding the conversion efficiency.^{2–4} Understanding the underlying mechanisms controlling the CS and CR dynamics is therefore central to a broad range of fundamental researches and applications.

In this work, we study the ultrafast excited-state relaxation dynamics, including CR, upon photoexcitation of a prototypical electron donor–acceptor (EDA) complex. One characteristic feature of EDA complexes is the appearance of a new absorption band, commonly attributed to an intermolecular charge-transfer (CT) transition, involving electron transfer from the donor to the acceptor.^{5–8} Mulliken described the ground and excited states of such complexes as linear combinations of the wave functions for the nonbonded and ion-pair states.⁵ The first CT absorption of EDA complexes usually corresponds to a transition from the HOMO localized

in the donor to the LUMO localized in the acceptor, resulting in an ion pair ($\text{D}^+–\text{A}^-$) with a high degree of CS.^{5,6} In response to the instantaneous and dramatic charge-distribution change, solvation and other relaxation processes take place rapidly to bring the system to a fully solvated equilibrium CT state, sometimes referred to as the “contact ion pair” (CIP).⁸ Competing with these relaxations are the charge recombination and dissociation into free ions. The CR reaction of the EDA complex CT state is equivalent to a back electron transfer (ET) that brings the system from the ionic excited state to the neutral ground state. Thus, the CT excitation of EDA complexes provides a unique opportunity for studying bimolecular ET reactions and has been used for this purpose extensively.^{8–13}

Although ET reactions in polar liquids are coupled more strongly to the solvation dynamics,¹⁴ the roles of intramolecular vibrational modes and their dynamics in ET have also been addressed both theoretically^{15–23} and experimentally.^{17,24–27} The success of the hybrid model of Barbara,^{17,24} which combines the merits of the Sumi–Marcus¹⁵ and the Bixon–

Received: May 9, 2013

Revised: July 10, 2013

Published: July 18, 2013

Jortner¹⁶ models, unequivocally indicated the importance of the coupled high-frequency as well as the low-frequency intramolecular vibrational modes, in addition to the solvent modes in ET dynamics. Recent theories^{20–23} have also shown that high-frequency vibrational modes can greatly accelerate ET dynamics. An interesting and challenging problem pertaining to these pictures is how fast the initial nonuniform vibrational distribution relaxes with respect to the time scales of ET and its effects on the ET rates.

Vertical excitation of an EDA complex into the CT state usually deposits a substantial vibrational energy in various FC active modes,^{28–30} including many intramolecular modes in D⁺ and A⁻ moieties as well as the low-frequency intermolecular D-A modes.^{28–30} Recent ultrafast time-resolved studies^{31–39} have revealed that, for medium to large molecular systems in solutions, intramolecular vibrational energy redistribution (IVR) can be nonstatistical even at high levels of excitation, and IVR time scales ranging from subpicosecond to a few picoseconds have been reported.^{31–39} Moreover, vibrational cooling (VC), that is, vibrational energy transfer through collisions with the solvent, takes an even longer time scale,^{35–41} and therefore, relaxation in the low-frequency vibrational modes can be expected to be on similar time scales of ET, even for systems with medium electronic couplings. In such cases, nonequilibrium ET with respect to the relaxation along low-frequency vibrational modes, instead of the solvent modes,^{21,42–44} must be considered. This is particularly important in EDA complexes because of the presence of many low-frequency intermolecular D-A modes. Unfortunately, vibrational relaxation in EDA complexes upon CT excitation has not been examined carefully in the past. A recent report by Fujisawa et al.⁴⁵ using femtosecond stimulated Raman spectroscopy to study an EDA complex has just begun to address this issue. The effect of nonequilibrium vibrations on ET between D and A through a molecular bridge has also been reported recently.⁴⁶

Another interesting aspect regarding vibrational relaxation in CT states of EDA complexes is the accompanied structural relaxation. Owing to the very different natures of D-A interactions in the ground and CT states, the equilibrium D-A structures of the CT state can be very different from that of the ground state. In such cases, vibrational relaxation following initial Franck-Condon (FC) excitation can lead to a substantial CT-state structural relaxation. Moreover, the CT-state structure may be subject to solvent perturbations, especially in high-polarity solvents, because of its highly ionic and floppy natures. Because electronic couplings are sensitive functions of the relative orientations and distances between D and A,^{47–49} such structural relaxation may bring about interesting dynamical effects on ET reactions.

The system of interest here is the EDA complex containing benzenes (BZ) as the donor and tetracyanoethylene (TCNE) as the acceptor. The series of EDA complexes containing TCNE and various methyl-substituted benzenes (MBZ) are among the earliest examples of EDA complexes^{6,50,51} and have been studied extensively.^{28,42,52–64} Among all MBZ-TCNE complexes, hexamethylbenzene-TCNE (HMB-TCNE) is probably the most intensively studied system both experimentally^{42,56–64} and theoretically.^{30,64–68} Surprisingly, compared with HMB-TCNE, the smallest member of the series, namely, the BZ-TCNE complex, has not been given much attention. Early studies of the BZ-TCNE complex in the vapor and liquid phases have focused on the thermodynamic

properties.^{50,51,69–71} To the best of our knowledge, the only available time-resolved data for BZ-TCNE is a transient-absorption study that reported a CR rate of $1.4 \times 10^{10} \text{ s}^{-1}$ in dichloromethane.⁷² Other time-resolved studies have focused on larger MBZ-TCNE systems.^{42,54,57–59} The relatively long CT-state lifetime of BZ-TCNE provides us with an opportunity to explore various relaxation processes along both solvent and vibrational coordinates as well as the solvent-dependent CR dynamics. Two unique features of the BZ-TCNE complex that may be distinctive from other members of MBZ-TCNE complexes are its higher symmetry and the lack of hindrance effect due to the absence of bulky methyl groups in the donor; both of which may bear important consequences on the CR dynamics.

In the past few decades, many spectroscopic techniques have been employed to investigate the CT-state dynamics of EDA complexes.^{11,42,45,56–64} In this study, we employed a broadband ultrafast time-resolved fluorescence (TRFL) spectrometer implemented by the optical Kerr gating (OKG) to study the BZ-TCNE CT-state dynamics. TRFL spectra directly reflect the excited-state distributions along solvent and vibrational coordinates and, therefore, are suitable for studying such relaxation processes. In our experiments, the CT state of the BZ-TCNE complex is directly reached via femtosecond laser excitation, and the resulting fluorescence is monitored with the OKG technique to measure the temporal and spectral evolutions of the fluorescence spectra, which carry detailed information on the subsequent relaxation dynamics. The fluorescence is quenched only by CR or dissociation into free ions. Thus, the observed TRFL spectra reveal a complete picture of the CT-state relaxation dynamics from the initial FC state to CR or dissociation. The solvents used in this study were dichloromethane (CH_2Cl_2), carbon tetrachloride (CCl_4), and cyclohexane ($c\text{-C}_6\text{H}_{12}$; CHX). By comparing and analyzing TRFL spectra obtained in solvents of different polarities, we partially separated the solvation and vibrational relaxation dynamics and explored the solvent dependence of CR dynamics.

2. EXPERIMENTAL SECTION

Apparatus. The ultrafast broadband TRFL spectrometer used in this work is based on the optical Kerr-gating technique and is similar to those described previously by other groups.^{73–75} The femtosecond laser system consists of a self-mode-locked Ti:sapphire laser (Spectra Physics, Tsunami) and a 1 kHz chirped-pulse regenerative amplifier (Spectra Physics, Spitfire). A fraction of the amplifier output at 766 nm was frequency-doubled in a thin BBO crystal to produce the excitation pulse at 383 nm. The remaining portion of the fundamental beam was used as the gate pulse. The Kerr shutter consists of a Kerr medium placed between a pair of crossed wire-grid polarizers (Moxtek, PPL04C). The excitation pulses excite sample solutions contained in a 2-in.-diameter rotating cell with 1-mm-thick fused-silica windows. The internal path length of the cell was either 0.5 mm (for BZ-TCNE in CH_2Cl_2) or 1 mm (for BZ-TCNE in CCl_4 and CHX). A half-wave plate was used to rotate the excitation-laser polarization at the “magic angle” with respect to the first polarizer of the Kerr shutter. The fluorescence was collected by a 90° off-axis 2-in.-diameter parabolic mirror with an effective focal length of 75 mm. The collected fluorescence was then directed through the first polarizer and focused on the Kerr medium by a second 90° off-axis parabolic mirror (effective $f = 150$ mm). The fluorescence

spot on the Kerr medium was about 1 mm² in size. The gate pulse was directed through a computer-controlled delay line and then steered to overlap with the fluorescence spot at the Kerr medium. The gate beam size was adjusted to match that of the fluorescence spot at the Kerr medium by using a focusing lens. The polarization of the gate pulse was rotated by 45° with respect to the first polarizer to maximize for the gating efficiency.^{73–75} The laser irradiance was adjusted by placing variable neutral density filters in the beam paths. Typical pulse energies used here were ~1 μJ/pulse for excitation and 50–75 μJ/pulse for the gate.

The gated fluorescence was collected and imaged onto the entrance slit of a spectrograph (Zolix, Omni-λ 300, 150 lines/mm grating) via a pair of achromatic lenses. A long-pass filter (CG-GG-400) and a short-pass filter (Omega Optical 728SP) filter were placed in front of the spectrograph to reject the scattered light. These cutoff filters determine the detection spectral range of the present setup (400–720 nm). The dispersed fluorescence spectra were recorded by a TE-cooled (−65 °C) CCD camera (Andor, DU970N-BV). For time-resolved experiments, “binning” over eight adjacent pixels covering about 2.8 nm of spectral range was performed prior to readout. The combination of the “binning” and the entrance slit width of 1 mm resulted in an effective spectral resolution of ~10 nm, as estimated from solvent Raman lines.

A computer program was devised to automate the data acquisition. The program stops the translation stage at a series of preselected positions and records the gated fluorescence spectra at the corresponding delay times by accumulating the electron counts on each CCD pixel. A background spectrum taken at a negative delay time, usually about −20 ps, was subtracted from the spectra measured at each delay time. Typically, TRFL spectra at 60–100 delay times were measured in each scan. To minimize long-term signal drifts, the program makes repetitive scans along both directions and averages the recorded spectra until a satisfactory signal-to-noise (S/N) ratio is achieved. Spikes due to cosmic ray are removed from each scan before averaging. Results of each repetitive scan were also saved for latter inspections of any long-term variation due to sample degradation. This capability has proved to be important because changes in spectral features do occur in some systems, including those presented in this work, after long hours of scanning. In such cases, only data accumulated prior to the appearance of these undesired changes were used.

The Kerr medium used in the present study is liquid benzene, which has been shown to provide a reasonable compromise between gating efficiency and temporal resolution.⁷⁴ For BZ–TCNE in CH₂Cl₂ experiments, liquid benzene placed in a cell of 0.5 mm internal path length was used as the Kerr medium. This gives an instrument response function (IRF) of ~0.35 ps in width (fwhm) as measured by the Raman response of a pure solvent (0.5 mm thick) (see the Supporting Information). For BZ–TCNE in CCl₄ experiments, the complex concentration was much lower (see below), and therefore, a 1-mm-thick liquid benzene was used as the Kerr medium to increase the gating efficiency. This deteriorated the temporal resolution to ~0.5 ps (with a 1-mm-thick sample). For the BZ–TCNE in CHX experiments, the complex concentration was even lower, and therefore, a 2-mm-thick liquid benzene was used as the Kerr medium, and the temporal resolution became ~0.75 ps (with 1-mm-thick sample). In other experiments in which higher temporal resolutions are needed, a 1-mm-thick fused-silica plate can be used as the Kerr

medium to obtain a better temporal resolution of ~0.21 ps at the cost of gating efficiency (see the Supporting Information). The Raman temporal responses of neat solvents were fit with model functions consisting of a Gaussian and a reversed exponential decay and were used as the IRF functions in the iterative deconvolution procedures described below.

Steady-state absorption spectra were measured with a UV-vis absorption spectrometer (Hitachi U-3900). Steady-state fluorescence spectra were recorded using the same setup described above for the TRFL experiments with the first Kerr-shutter polarizer removed and the gate beam blocked. The short-pass filter was also removed in this case. Steady-state spectra were recorded with a smaller entrance slit and without pixel binning, resulting in an effective spectral resolution of ~3 nm. All experiments were carried out at room temperature (~23 °C).

Samples. TCNE was purchased from Aldrich (98%) and was sublimed twice before use. CH₂Cl₂ (Baker, 99.9%) and CHX (Merck, Uvasol grade, 99.9%) were used as received, and CCl₄ (Showa, 99.5%) was fractionally distilled before use. For the BZ–TCNE in CH₂Cl₂ experiments, the nominal concentrations of the acceptor and the donor (BZ) are $c_{\text{TCNE}} = 2.0 \times 10^{-2}$ M and $c_{\text{BZ}} = 2.0 \times 10^{-1}$ M, respectively; that is, a donor-to-acceptor concentration ratio ($c_{\text{D}}/c_{\text{A}}$) of 10. The optical density (OD) of this solution at the peak of the CT absorption band is ~0.08 (path length = 0.5 mm). Because of the much lower solubility of TCNE in CCl₄ and in CHX, the nominal concentrations were reduced to $c_{\text{TCNE}} = 1.6 \times 10^{-3}$ M and $c_{\text{BZ}} = 4.0 \times 10^{-2}$ M in CCl₄ ($c_{\text{D}}/c_{\text{A}} = 25$) and $c_{\text{TCNE}} = 7.7 \times 10^{-4}$ M and $c_{\text{BZ}} = 1.9 \times 10^{-2}$ M in CHX ($c_{\text{D}}/c_{\text{A}} = 25$). The ODs (1.0 mm path length) at the peak of the CT absorption band were ~0.02 for the CCl₄ solution and 0.006 for the CHX solutions, respectively. Sample solutions were freshly prepared before all experiments presented here.

Spectral Sensitivity and Temporal Dispersion Corrections. Procedures used to correct for spectral sensitivity and temporal dispersion of the measured TRFL spectra are described in the Supporting Information.

3. RESULTS AND DATA ANALYSES

3.1. Steady-State Absorption and Fluorescence Spectra.

Figure 1 shows the steady-state absorption and

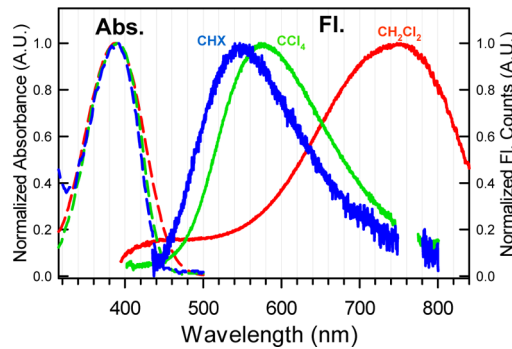


Figure 1. Steady-state absorption (dashed lines) and fluorescence (solid lines) spectra of the BZ–TCNE complex in CHX (blue), CCl₄ (green), and CH₂Cl₂ (red). The fluorescence spectra were corrected for the spectral sensitivity. Raman lines and stray light signals due to scattered gate pulse at about 766 nm have been removed (CH₂Cl₂) or deleted (CCl₄ and CHX). The concentrations of the solutions are those stated in the Experimental Section.

Table 1. Solvent Properties and Spectral Characteristics of BZ–TCNE and C153

| solvent ^a | solvent properties ^b | | | | steady-state characteristics ^c | | | time-dependent characteristics ^d | | | | |
|---------------------------------|---------------------------------|------------|---------|---------|---|-------------------|-------------|---|---------------------|---------------------|-----------------------------|------|
| | μ | ϵ | π^* | E_N^T | ν_{abs} | ν_{em} | $\delta\nu$ | $\delta\nu$ | $\bar{\nu}(0)$ | $\bar{\nu}(\infty)$ | $\Delta\bar{\nu}_{0\infty}$ | |
| CH ₂ Cl ₂ | 1.14 | 8.9 | 0.82 | 0.309 | 25700 | 13000 | 12700 | 5060 | 20300 | 13000 | 7300 | 1110 |
| CCl ₄ | 0.00 | 2.3 | 0.21 | 0.052 | 25700 | 16930 | 8770 | 4160 | 20000 | 16500 | 3500 | 300 |
| CHX | 0.00 | 2.0 | 0.00 | 0.006 | 25800 | 17800 | 8000 | 4230 | ~20000 ^f | 17500 | ~2500 ^f | -40 |

^aCHX denotes cyclohexane. ^bDipole moments (μ) in Debye and static dielectric constants (ϵ) are for 25 °C. The solvatochromic polarity scales π^* values are from refs 97 and 98, and E_N^T values are from ref 96. ^c ν_{abs} and ν_{em} are peak frequencies of the steady-state absorption and emission spectra. $\delta\nu$ is the Stokes shift. All frequencies are in cm⁻¹. ^d $\bar{\nu}(0)$ is the mean emission frequency near time zero derived from the observed TDFSS data with the deconvolution procedure described in the text; $\bar{\nu}(\infty)$ is the mean emission frequency at long delay time where the spectral relaxation ceases; $\Delta\bar{\nu}_{0\infty}$ is the magnitude of the dynamic Stokes shift defined as $\bar{\nu}(0) - \bar{\nu}(\infty)$; $\Delta\bar{\nu}_{10\infty}$, taken from ref 89, is the estimate of the magnitude of dynamic Stokes shifts of C153 using the “time-zero” spectrum approach. All frequencies are in cm⁻¹. ^eAll C153 data are from ref 89. ^fEstimated values.

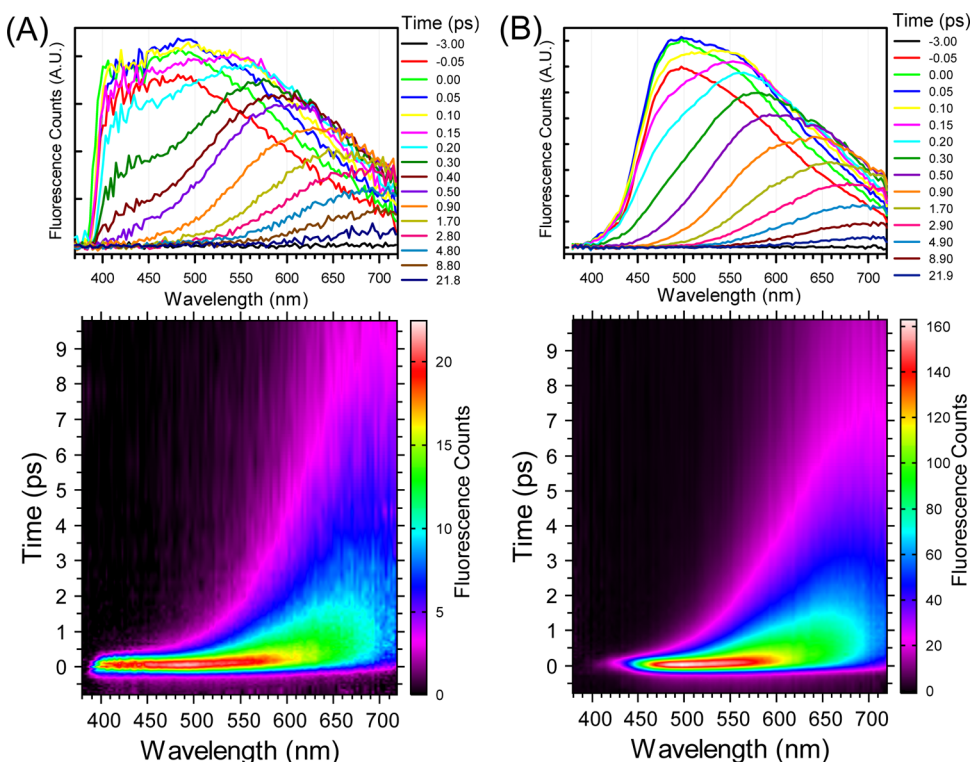


Figure 2. (A) Time- and spectral-sensitivity-corrected TRFL spectra of BZ–TCNE in CH₂Cl₂ at low concentrations ($c_{\text{TCNE}} = 0.02$ M and $c_{\text{BZ}} = 0.2$ M; $\text{OD}_{390\text{ nm}} = 0.08$) with 383 nm excitation. Spectral features due to Raman scatterings have been removed. Upper panel shows selected TRFL spectra at some representative delay times, and the lower panel shows the early time portion of the contour plot. (B) Time- and spectral-sensitivity-corrected TRFL spectra of BZ–TCNE in CH₂Cl₂ at high concentrations ($c_{\text{TCNE}} = 0.083$ M and $c_{\text{BZ}} = 0.83$ M; $\text{OD}_{390\text{ nm}} = 1.2$) with 383 nm excitation. Spectral features due to Raman scatterings have been removed. The much higher OD substantially suppressed the fluorescence in the blue region ($\lambda < 450$ nm) due to the inner filter effect while leaving spectral characteristics in other regions unchanged with a much better S/N.

fluorescence spectra of BZ–TCNE complex in the three solvents studied in this work. The absorption spectra of BZ–TCNE complex in these solvents are very similar, with maxima located near 390 nm. The widths of absorption spectra in nonpolar solvents (CCl₄ and CHX) are slightly narrower than that in CH₂Cl₂, suggesting a steeper excited-state energy dependence on the solvation coordinates in polar solvents.⁷⁶ In sharp contrast to the absorption spectra, the steady-state fluorescence spectra in these solvents are quite different. The fluorescence in CH₂Cl₂ exhibits a much larger red shift than those observed in the nonpolar solvents, consistent with the expected CT nature of the BZ–TCNE excited state. The fluorescence spectra were converted to frequency domain using $I(\nu) = I(\lambda) \lambda^2$, and the Stoke shifts measured in these three solvents are listed in Table 1. Justifications of the assignment of

these steady spectra and the TRFL spectra discussed below to the BZ–TCNE 1:1 complex are given in the Supporting Information.

3.2. TRFL Spectra of BZ–TCNE in CH₂Cl₂, CCl₄, and CHX. We have measured TRFL spectra of the BZ–TCNE complex in CH₂Cl₂, CCl₄, and CHX with 383 nm excitation, and the results after spectral-sensitivity and time corrections using the procedures described in the Supporting Information are displayed in Figures 2, 3, and 4, respectively. For the sake of clarity, only TRFL spectra at some representative delay times are shown. Sharp spectral features due to Raman scattering have been removed from these spectra.⁷⁷ These corrected TRFL spectra are also displayed in Figures 2–4 as contour plots for shorter time scales.

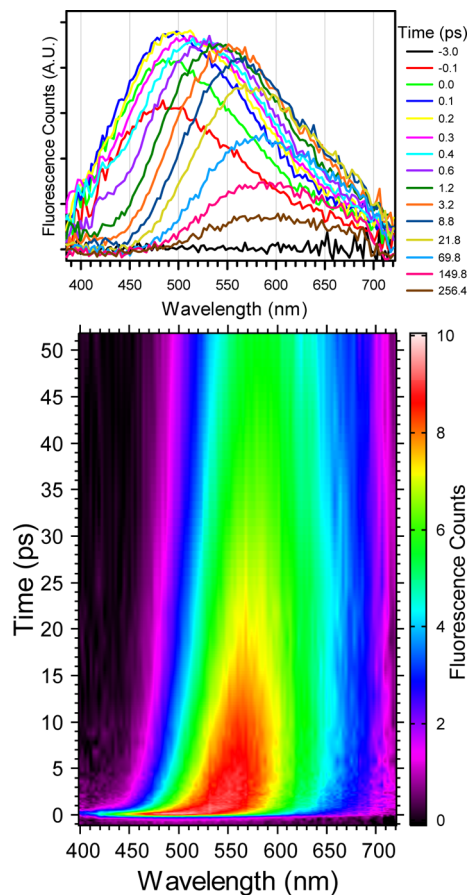


Figure 3. Time- and spectral-sensitivity-corrected TRFL spectra of BZ-TCNE in CCl_4 excited at 383 nm. Spectral features due to Raman scatterings have been removed. Upper panel: selected TRFL spectra at some representative delay times. Lower panel: early time portion of the contour plot.

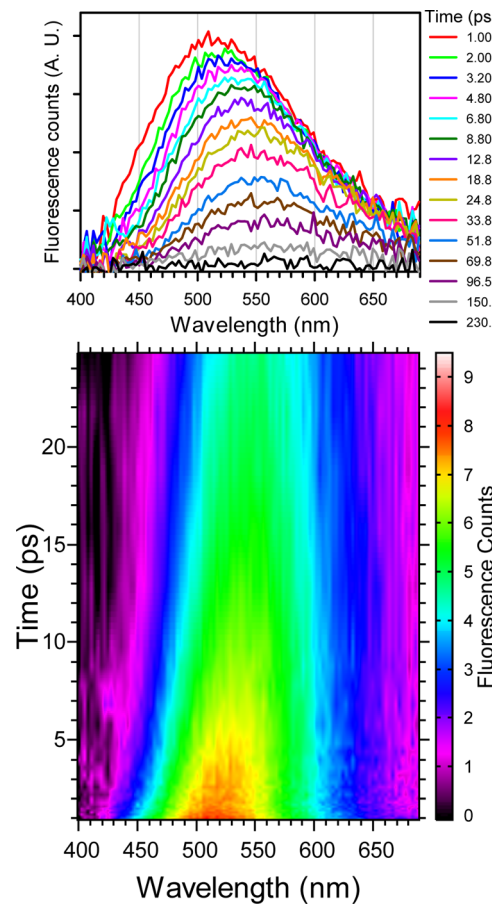


Figure 4. Time- and spectral-sensitivity-corrected TRFL spectra of BZ-TCNE in CHX excited at 383 nm. Upper panel: selected TRFL spectra at some representative delay times. Lower panel: early time portion of the contour plot. The data before 1 ps are not available in this case because of strong interferences from the solvent Raman signal.

The results shown in Figure 2A clearly reveal that upon CT excitation in CH_2Cl_2 , the BZ-TCNE emission undergoes a rapid spectral relaxation to the red. A spectral feature in the blue region between 400 to 450 nm distinctive from the rest of the emission is evident. The overall fluorescence intensity also decays rapidly along with the spectral relaxation, making spectral characterization difficult at longer delay times. To circumvent this problem, we have also measured TRFL spectra with much higher donor and acceptor concentrations ($c_{\text{TCNE}} = 0.083 \text{ M}$ and $c_{\text{BZ}} = 0.83 \text{ M}$), and the results are shown in Figure 2B. Although the higher complex concentration enhanced the S/N ratio substantially, the much higher OD of this solution (~ 1.2 at λ_{max} for a 0.5 mm path length) resulted in a sizable inner filter effect that greatly diminished the blue emission. Nevertheless, as can be seen in Figure 2A and B, the spectral characteristics of the high-concentration TRFL spectra beyond ~ 2 ps remain nearly identical to the low-concentration ones but with higher S/N ratios. The high-concentration spectra allowed more accurate characterizations of the fluorescence dynamics beyond 2 ps and were used for this purpose in the following analyses.

At ~ 8 ps, the maxima of TRFL spectra reach the short-pass-filter cutoff at ~ 720 nm. To observe spectral dynamics beyond 8 ps, we also measured TRFL spectra of BZ-TCNE in CH_2Cl_2 with 415 nm excitation. In this case, the short-pass filter can be replaced by one that cuts off at a longer wavelength of ~ 770

nm, allowing the maxima of TRFL spectra to be detected at longer delay times. Unfortunately, the long-pass filter used for rejecting the excitation scattered light also had to be replaced, from one that cuts off at 400 nm to one at 430 nm, which limits the detection of blue emission for early time (< 0.5 ps) spectra. However, the TRFL spectra obtained with 415 and 383 nm excitations were found to be nearly identical beyond ~ 3 ps. Therefore, the data obtained with 415 nm excitation were used for spectral analyses beyond 8 ps. For easy comparison, the TRFL spectra at 11 representative delay times, taken from the three separated experiments stated above, are scaled to the same height and plotted in Figure 5A in frequency scale along with the steady-state fluorescence and absorption spectra.

These TRFL spectra contain rich information regarding the relaxation dynamics of the BZ-TCNE complex upon CT excitation. Although the steady-state fluorescence spectrum in CH_2Cl_2 is shifted largely to the red, the initial TRFL spectra measured immediately after excitation peak in the green spectral region and are quite broad and asymmetric. The TRFL spectra exhibit an extremely rapid spectral relaxation within the first ~ 1 ps, followed by a much slower evolution. The widths of TRFL spectra also become narrower along with this rapid spectral relaxation.

TRFL spectra were also measured for BZ-TCNE complex in CCl_4 with 383 nm excitation (see Figure 3). Limited by the low

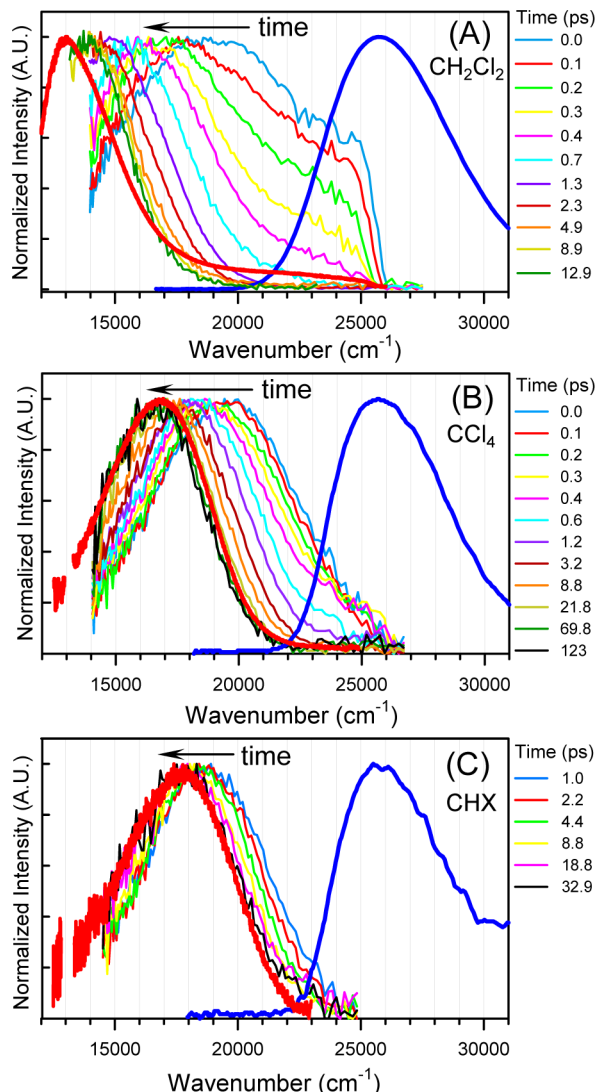


Figure 5. TRFL spectra (thin colored lines) of BZ–TCNE excited at 383 nm in the three solvents presented in the wavenumber (cm^{-1}) scale at some representative delay times: (A) in CH_2Cl_2 , (B) in CCl_4 , and (C) in CHX. The steady-state absorption (blue thick lines) and fluorescence spectra (red thick lines) are also shown for comparison. All TRFL spectra are time- and spectral-sensitivity-corrected and are scaled to the same maximum intensity. The last two TRFL spectra ($t = 8.9$ and 12.9 ps) in CH_2Cl_2 were taken from data measured with 415 nm excitation for reasons described in the text. Note that the fwhm's of effective IRFs in the three cases are 0.35 (CH_2Cl_2), 0.5 (CCl_4), and 0.75 ps (CHX).

solubility of TCNE in CCl_4 ($<2 \times 10^{-3}$ M), the BZ–TCNE complex concentration is very low ($\sim 5.5 \times 10^{-5}$ M) in this case. Therefore, a 1-mm-thick liquid benzene Kerr medium and 1-mm-thick sample solution were used to improve the S/N. This resulted in a broader effective IRF of ~ 0.5 ps (fwhm). As expected, the TRFL spectra in CCl_4 exhibit a much smaller spectral relaxation than those observed in CH_2Cl_2 . Nevertheless, spectral relaxation still can be clearly observed, even beyond 10 ps. Figure 5B shows TRFL spectra at 12 representative delay times that are scaled to the same height along with the steady-state fluorescence and absorption spectra in frequency scale. It can be clearly seen that the TRFL spectra also exhibit a rapid spectral relaxation within the first picosecond, followed by a much slower and milder relaxation.

Beyond ~ 50 ps, the TRFL spectra merely decay with time without noticeable variations in positions and shapes.

TRFL spectra for the BZ–TCNE complex in CHX were also measured with 383 nm excitation. In this case, the complex concentration is even lower because of very low solubility of TCNE in CHX, and therefore, a 2-mm-thick liquid benzene Kerr medium was used, resulting in an effective IRF of ~ 0.75 ps in fwhm (with 1-mm-thick sample solution). Unfortunately, owing to the very low complex concentration and the very strong Raman scatterings of CHX, the Raman bands are relatively intense in this case and cannot be reliably subtracted from the TRFL spectra.⁷⁸ Therefore, only data after 1 ps were included in the analysis. The results after spectral sensitivity and time corrections are shown in Figure 4 for $t > 1$ ps. Figure 5C shows TRFL spectra that are scaled to the same height at several representative delay times, along with the steady-state fluorescence and absorption spectra in frequency scale. CHX is usually not expected to produce observable spectral relaxation for typical solvation probes, such as C153.⁷⁹ Nevertheless, the TRFL spectra of BZ–TCNE in CHX clearly exhibit a small but nonnegligible spectral relaxation within the first 20 ps. Beyond ~ 30 ps, the TRFL spectra merely decay with time without variations in positions and shapes.

3.3. Fluorescence Transients. The fluorescence transients (time traces) can be extracted directly from the corrected TRFL data by plotting the fluorescence intensity at the wavelength of interest as a function of time. Transients at several representative spectral regions are displayed in Figure 6A and B for BZ–TCNE in CH_2Cl_2 and CCl_4 , respectively. These transients were fit to the convolution of the IRF and a multiexponential function using an iterative deconvolution procedure, and the results are also shown in Figure 6 (solid lines). At least five exponential components are needed to satisfactorily describe all transients observed in CH_2Cl_2 , whereas four components are enough to fit the data in the CCl_4 case. Time constants of all these components are found to be wavelength-dependent except for the shortest ones, which must be fixed at reasonable estimated values. The numbers of components needed to fit these transients and their variations with wavelength indicate the complexity of the dynamics involved.

At the very blue end of the TRFL spectra ($\lambda_{\text{em}} < 450$ nm), the fluorescence is dominated by an extremely fast decay (<0.1 ps). In the longer wavelength regions, slower temporal components gradually grow in. The systematic variations of the transients with the emission wavelengths simply reflect the temporal evolutions of spectral characteristics. Various processes, such as solvation, vibrational relaxation, and electronic transitions, occur simultaneously, and all contribute to the time-dependent fluorescence signal at a particular wavelength. Some of them occur in very similar time scales, making it difficult to identify these entangled temporal components from the fluorescence transients. For this reason, the following analyses will focus on evaluating the temporal evolution of spectral characteristics of TRFL spectra as a whole.

These fluorescence transients should be compared with those reported by Rubtsov and Yoshihara^{58,59} for HMB–TCNE complex using a femtosecond fluorescence up-conversion gating technique. With a much better temporal resolution of ~ 80 fs, they observed an oscillatory fluorescence decay with a period of 215 fs (155 cm^{-1}) when exciting a HMB–TCNE complex in CCl_4 solution into its CT band. They concluded that an out-of-plane vibrational mode of the acceptor anion

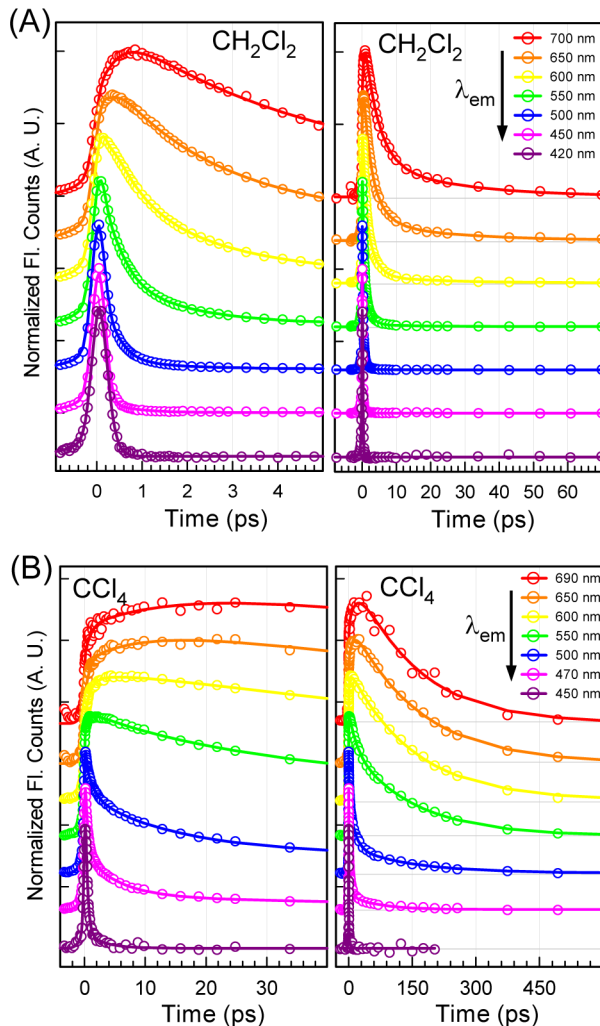


Figure 6. Fluorescence transients extracted from the TRFL spectra presented in Figure 2 and 3 at several representative wavelengths for BZ–TCNE excited at 383 nm in (A) CH_2Cl_2 and (B) CCl_4 . Each trace is the average of data over a ~ 10 nm spectral window centered at the denoted wavelength. The colored solid lines are the best fits of a multiexponential model function convoluted with the IRF to the data (colored circles).

(TCNE^-) is responsible for the observed oscillations.⁵⁹ It is not surprising that such a fast oscillatory component was not resolved in the transients shown in Figure 6 because the effective temporal resolutions in the present setup (0.35–0.75 ps) were not high enough.

3.4. Data Analyses. To unveil the underlying dynamics in the TRFL spectra, we examined the time dependence of several TRFL spectral properties as described below. First, the time-dependent mean emission frequency (the first moment) was evaluated with

$$\bar{\nu}(t) = \frac{\int \nu \cdot I(\nu, t) d\nu}{\int I(\nu, t) d\nu} \quad (1)$$

where $I(\nu, t)$ represents the observed TRFL spectra after spectral sensitivity and time corrections. The time-dependent fluorescence dynamic Stokes shift (TDFSS) is then defined as $\delta\nu(t) = \bar{\nu}(t) - \bar{\nu}(\infty)$. The accurate evaluations of $\bar{\nu}(t)$ require integrations over the entire fluorescence spectral range. However, a portion of the BZ–TCNE fluorescence appears

in the region beyond the red edge of the spectral detection window, especially for those that emit at later times. To estimate the spectra in the undetected region, we extrapolated the observed TRFL spectra by fitting to a log-normal line shape function or, in some cases, a combination of two. The log-normal function is of the form

$$g(\nu) = A \cdot \exp \left\{ \left(-\ln 2 \right) \left(\frac{\ln(1 + \alpha)}{\gamma} \right)^2 \right\}, \alpha \geq -1 \\ = 0, \alpha < 1 \quad (2)$$

$$\alpha = 2\gamma(\nu - \nu_p)/\Omega$$

where ν_p is the peak frequency, Ω is the width parameter, and γ is the asymmetry parameter. The evaluation of $\bar{\nu}(t)$ was then performed with the results obtained from the log-normal function fittings. For TRFL spectra measured in CH_2Cl_2 and CCl_4 , it is necessarily to use a linear combination of two log-normal functions to fit the early time (<1 ps) spectra. The results are shown in Figure 7 for BZ–TCNE in the three solvents studied here. This procedure worked quite well for TRFL spectra measured in CCl_4 and CHX because only small

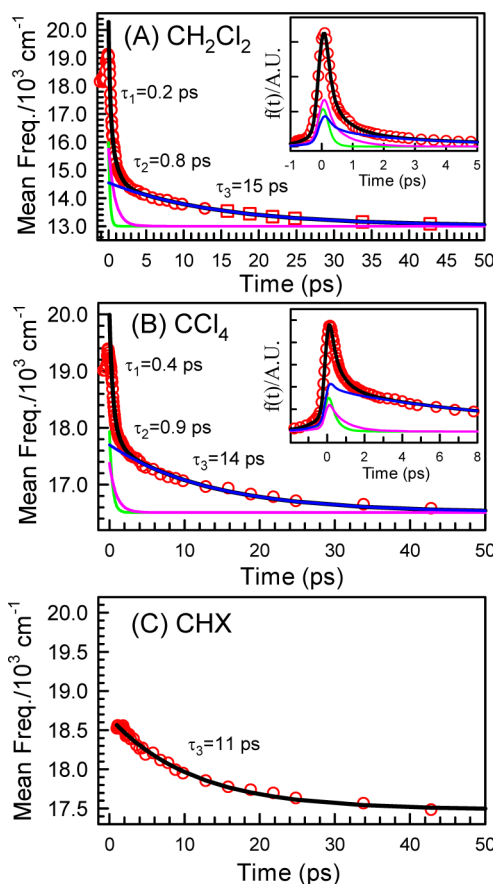


Figure 7. Temporal evolutions of mean emission frequency, $\bar{\nu}(t)$, of BZ–TCNE excited at 383 nm in the three solvents: (A) CH_2Cl_2 , (B) CCl_4 , and (C) CHX. The black solid lines are the deconvoluted results, that is, $\bar{\nu}^*(t)$, using the procedures described in the text, and the thin colored lines are the decomposed components. The insets in A and B show the corresponding $f(t)$ functions and the fitting results used in the deconvolution procedures. Only data for $t > 1$ ps are shown in C for the CHX case. Note the different frequency and time scales of these three graphs.

portions of the spectra were not detected. On the other hand, in CH_2Cl_2 , a substantial spectral portion was not detected for TRFL spectra beyond 1 ps, and therefore, some constraints on the fitting parameters must be imposed to obtain reliable fits. First, the TRFL spectra beyond 1 ps were assumed to be nearly symmetric, with $\gamma = -0.01$. This allows stable fittings up to ~ 13 ps (open circles in Figure 7A) with the 415 nm excitation data. It is then evident (see Figure 7A) that the spectral relaxation is multiexponential and that a distinctive slow component is present beyond ~ 3 ps. To characterize the TRFL spectra beyond 13 ps, we simply fit the $\bar{\nu}(t)$ data between 3 and 13 ps with a single exponential decay under the constraint that $\bar{\nu}(t)$ converges to the peak frequency of the steady-state emission spectrum at 13000 cm^{-1} . Finally, the TRFL spectra beyond 13 ps were fit to log-normal functions with the peak frequencies (ν_p) fixed at the extrapolated values (open squares in Figure 7A).

$\bar{\nu}(t)$ serves as a convenient measure for the spectral relaxation after excitation; however, each observed TRFL spectrum is a time integration of the fluorescence within the temporal detection window. This obscures the time dependence of emission frequency, especially for the very early time region, where the spectral relaxation is expected to be very rapid. We employed a procedure suggested by Gutavaason et al.⁸⁰ to partially remove this broadening effect. Briefly, a new function, $f(t) = J(t) \delta\bar{\nu}(t)$, where $J(t) = \int I(\nu, t) d\nu$, was calculated using the results from the log-normal-function fittings. $J(t)$ is simply the time dependence of the total fluorescence intensity. $f(t)$ was then fit with the product of two multiple-exponential model functions, $J^*(t) \delta\bar{\nu}^*(t)$, convoluted with the IRF using an iterative deconvolution procedure. $J^*(t)$ is the deconvoluted function of $J(t)$ and can be obtained from fitting $J(t)$ with a multiple-exponential model functions. $\delta\bar{\nu}^*(t)$ is the deconvoluted function of $\delta\bar{\nu}(t)$ to be obtained from fitting $f(t)$. The desired deconvoluted function of $\bar{\nu}(t)$ was then obtained by adding the relaxed mean emission frequency to $\delta\bar{\nu}^*(t)$, that is, $\bar{\nu}^*(t) = \delta\bar{\nu}^*(t) + \bar{\nu}(\infty)$. The results of these fittings are shown in Figure 7A and B for BZ-TCNE in CH_2Cl_2 and CCl_4 , respectively. The corresponding $f(t)$ used for fitting $\bar{\nu}(t)$ are displayed in the insets. In the case that CHX is the solvent, the data before 1 ps are not available, and therefore, the $\bar{\nu}(t)$ was simply fit with a single exponential decay for the slowest component. The time constants and magnitudes of decomposed components obtained from the fits are summarized in Table 2.

The time dependence of the TRFL spectral bandwidth is another important characteristic of spectral relaxation.^{81,82}

Table 2. Time Constants and Magnitudes of the Multiexponential Components Obtained from the Deconvolution Fittings of the BZ-TCNE TDFSS Data in Three Solvents

| | CH_2Cl_2 | CCl_4 | CHX |
|----------------------------|--------------------------|----------------|-------------------|
| τ_1 (ps) | 0.2 ± 0.1 | 0.4 ± 0.1 | N.A. ^b |
| A_1 (cm^{-1}) | 3000^a | 1400 | |
| τ_2 (ps) | 0.8 ± 0.1 | 0.9 ± 0.1 | |
| A_2 (cm^{-1}) | 2750 | 900 | |
| τ_3 (ps) | 15 ± 5 | 14 ± 1 | 11 ± 1 |
| A_3 (cm^{-1}) | 1550 | 1200 | ~ 1000 |

^aErrors in all dynamic Stoke shifts are about $\pm 100 \text{ cm}^{-1}$. ^bUnresolved subpicosecond components.

Figure 8 shows the temporal evolution of the full width at half-maximum (fwhm), $W(t)$, derived from the log-normal-

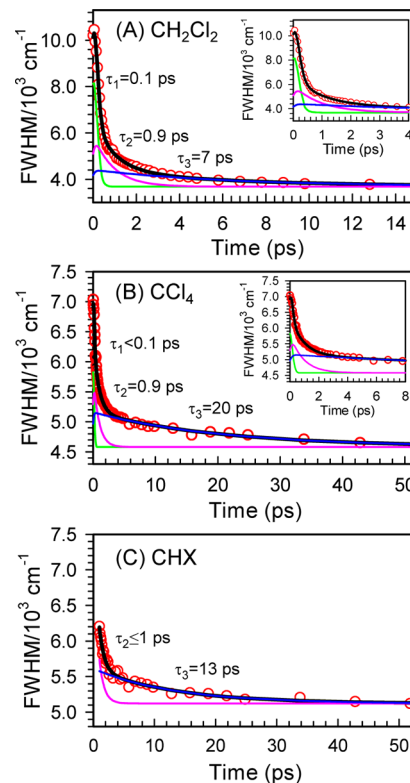


Figure 8. Temporal evolutions of fluorescence spectral bandwidth, $W(t)$, of BZ-TCNE excited at 383 nm in the three solvents: (A) CH_2Cl_2 , (B) CCl_4 , and (C) CHX. The black solid lines are the best fits of a multiexponential function convoluted with the IRF to the data, and the thin colored lines are the decomposed components. The insets show the same data in shorter time scales. Only data for $t > 1 \text{ ps}$ are shown in C for the CHX case. Note the different frequency and time scales of these three graphs.

function fittings of the corrected TRFL spectra. These data were analyzed by simply fitting $W(t)$ with a triexponential model function convoluted with the IRF; the results are summarized in Table 3.

Another useful characterization of the TRFL spectra is the total fluorescence intensity with the cubic-frequency correction, that is,

$$P(t) = \int \frac{I(\nu, t) d\nu}{\nu^3} \quad (3)$$

This function approximately reflects the temporal evolution of total excited-state population and the square of emission electronic transition moment.^{59,83,84} Again, $P(t)$ was evaluated with the results obtained from log-normal-function fittings of the experimental $I(\nu, t)$. Figure 9 shows the $P(t)$ for BZ-TCNE in three solvents along with the best fits to multiexponential functions convoluted with the IRFs.

3.5. TRFL Spectra of C153 in CH_2Cl_2 and CCl_4 . To identify the relaxation components due to polar solvation, we have also measured TRFL spectra of Coumarin 153 (C153) in CH_2Cl_2 and CCl_4 using the same experimental setup. C153 is probably the most popular solvation probe because of its large dipole moment change (6–8 D)^{79,80,85–89} upon excitation and rigid structure. The latter ensures that no intramolecular

Table 3. Time Constants of Multiexponential Components Obtained from Iterative Reconvolution Fittings of the BZ–TCNE $W(t)$ and $P(t)$ Data in Three Solvents

| | CH ₂ Cl ₂ | | CCl ₄ | | CHX | |
|------------|---------------------------------|-----------|------------------|--------------------|----------|----------|
| | $W(t)^a$ | $P(t)^b$ | $W(t)^a$ | $P(t)^b$ | $W(t)^a$ | $P(t)^b$ |
| τ_1^c | ~0.1 | <0.1 | <0.1 | <0.1 | | |
| τ_2 | 0.9 ± 0.1 | | 0.9 ± 0.1 | | | |
| τ_3 | 7 ± 1 | 3.2 ± 0.2 | 20 ± 2 | 5 ± 1 ^d | 13 ± 1 | |
| τ_4 | | 29 ± 1 | | 150 ± 2 | | 68 ± 2 |

^aFull width at half-maximum (fwhm). ^bTotal fluorescence intensity with cubic frequency correction. ^cAll time constants are in picoseconds. ^dThe rise component.

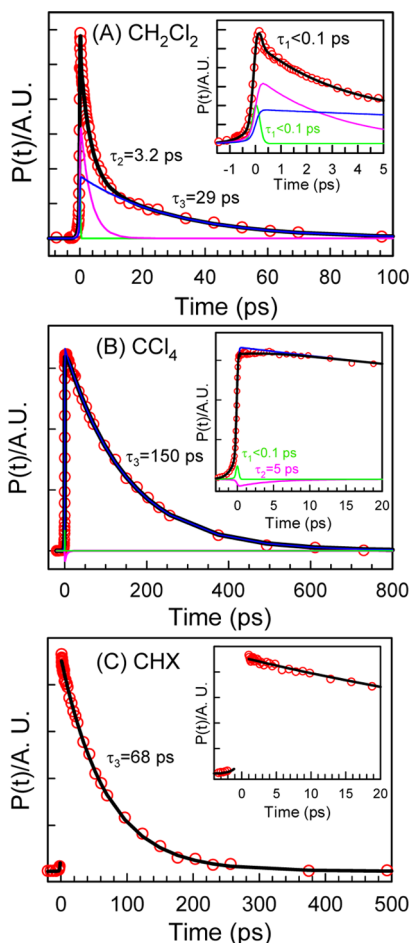


Figure 9. Temporal evolutions of the total fluorescence intensity with cubic frequency correction, $P(t)$, as defined in the text. The black solid lines are the best fits of a multiexponential function convoluted with the IRF to the data, and the thin colored lines are the decomposed components. The insets show the same data in shorter time scales. Only data for $t > 1$ ps are shown in C for the CHX case. Note the different frequency and time scales of these three graphs.

relaxation processes other than vibrational relaxation are involved in the observed TDFSS. Moreover, it is usually assumed that IVR in this system is much faster than 0.1 ps and that the spectral relaxation observed is due solely to polar solvation. The purpose for measuring TRFL spectra of C153 here is to provide a direct comparison with results obtained for BZ–TCNE using the same experimental setup. Figure 10 shows the contour plots of the TRFL spectra of C153 in CH₂Cl₂ and CCl₄ with 383 nm excitation after spectral sensitivity and time corrections. It is clear from these data that, in CH₂Cl₂, the system undergoes a rapid but mild spectral

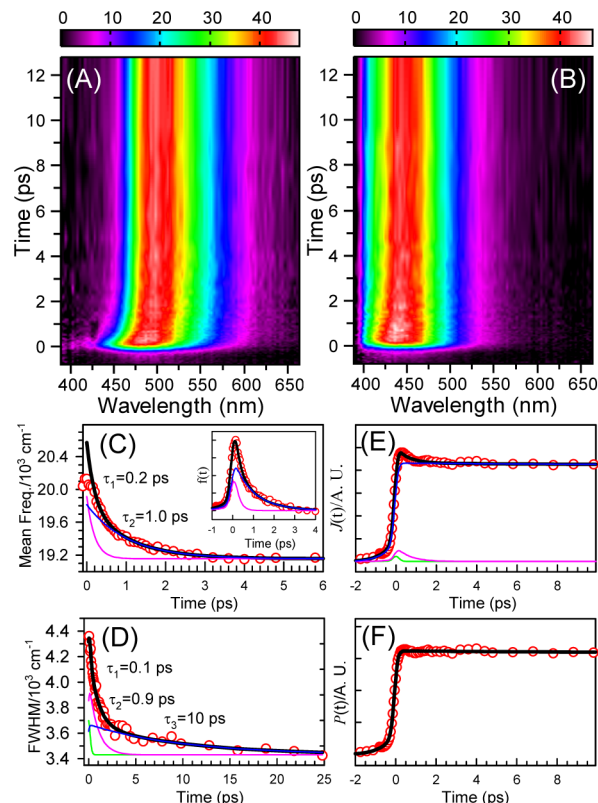


Figure 10. Contour plots of TRFL spectra of C153 excited at 383 nm in (A) CH₂Cl₂ and (B) CCl₄ after time and spectral sensitivity corrections. These data were taken with an effective IRF of 0.35 ps in fwhm. (C–F) Temporal evolutions of spectral characteristics of C153 in CH₂Cl₂.

relaxation within the first picosecond, whereas in CCl₄, very little spectral relaxation is present. Temporal evolutions of spectral properties obtained with the same data analysis procedures described above are also displayed in Figure 10 for the CH₂Cl₂ case. We will discuss the significance of these results below along with the BZ–TCNE data.

3.6. Electronic Structure Calculations: BZ–TCNE Ground and CT States. We have also carried out electronic structure calculations to provide some insights into the structures and energetics of the BZ–TCNE complex. All calculations described here were performed using the Gaussian 09 program.⁹⁰

3.6.1. Ground-State Structures and Energetics. We carried out DFT calculations with the M06-HF functional, which has been shown to lead to good performances in TDDFT calculations for CT excited states.⁹¹ The ground-state structure was first optimized at the M06HF/cc-pVTZ level of theory.

Two optimized structures, shown in Figure 11, were identified, both of which assume a parallel face-to-face C_{2v} structure with

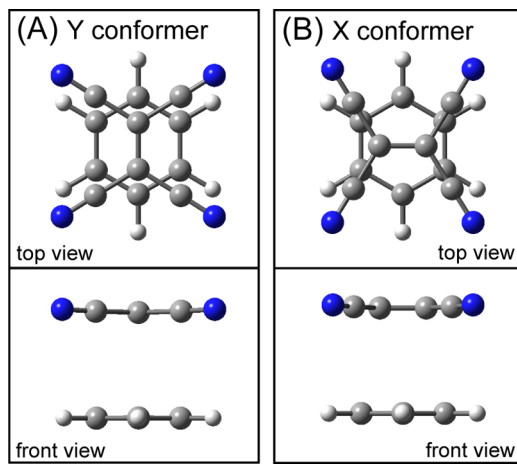


Figure 11. Two optimized ground-state structures of the BZ–TCNE complex at the M06H/cc-pVTZ level of theory: (A) the Y conformer and (B) the X conformer. The top panel is the top view, and the bottom panel is the front view of the same conformer. The interplanar distance is ~ 0.3 nm in both conformers.

the TCNE C=C bond either parallel or perpendicular to the C–C axis connecting the para carbon atoms in the benzene ring. The former is denoted as the Y conformer (parallel), and the latter the X conformer (perpendicular). The vibrational frequencies calculated at these two structures gave no imaginary frequency, indicating that they correspond to the true minima at this level of theory. The two structures are nearly isoenergetic, with the Y conformer being more stable than the X conformer by merely 0.0017 eV. The interplanar distances (R_{DA}) and the ground-state dipole moments (μ_{DA}) are very similar for both conformers (see Table 4). These results agree in general with a few previous computational studies of the BZ–TCNE complex,^{65–68,92} except that the interplanar distance calculated here is somewhat shorter.⁶⁸ Very recently, Kuchenbecker and Jansen⁶⁷ reported high-level ab initio calculations on the BZ–TCNE complex. At the CCSD(T*)-F12a level of theory, the Y conformer was reported to be more stable than the X structure by only 0.18 kJmol⁻¹. Through variation of the rotation angle at the fixed-monomer DFT-SAPT level of theory, they found that the X structure corresponds to a saddle point. The best estimate for the CCSD(T) interaction energy was 37.5 kJmol⁻¹.⁶⁷ Although some discrepancies exist, the extremely small energy differences

between the two structures concluded in both studies suggest that they must exist in almost equal populations at room temperature. This is in contrast to cases in which MBZs are the donor. For example, the barrier to rotation in *p*-xylene–TCNE was predicted to be a few kilojoules per mole.⁶⁷

A list of the low-frequency (< 200 cm⁻¹) vibrational modes calculated for the Y conformer is given in the Supporting Information. Frequencies of the corresponding modes of both conformers are very similar. The three lowest frequency modes (22.8, 69.7, and 71.1 cm⁻¹) correspond to symmetry-breaking intermolecular motions (see the Supporting Information), implying that the intermolecular potential energy surface (PES) is quite shallow along these coordinates. The combination of these results suggests that, although the BZ–TCNE complex is relatively strongly bound (37.5 kJmol⁻¹),⁶⁷ it does not have a well-defined structure at room temperature and can undergo facile large-amplitude intermolecular vibrational motions sampling a wide range of configurations.

3.6.2. Vertical Excitation Energies. We also carried out single-point time-dependent DFT calculations for the optimized ground-state structures described above at the TD-M06HF/cc-pVTZ level of theory. The results are summarized in Table 4 for the first two nearly degenerate singlet excited states corresponding to HOMO- and HOMO-1-to-LUMO excitations. The HOMO and HOMO-1 localize mainly in the benzene moiety, whereas the LUMO resides mostly in TCNE (see the Supporting Information). Accordingly, these two states are clearly due to BZ-to-TCNE CT excitation. The energy difference between these two CT states is less than 900 cm⁻¹ at the C_{2v} FC configuration. This is well understood because the HOMO and HOMO-1 in the complex originate from the doubly degenerate HOMOs in isolated benzene, which are split into two closely lying MOs under the influence of TCNE in the complex. Dual CT transitions can be clearly observed in absorption spectra of TCNE complexes with MBZs of lower symmetries, for example, *p*-xylene and durene,⁵¹ because the double degeneracy is more strongly removed intrinsically in these donors. The calculated vertical excitation energy is about 0.7 eV higher than the observed absorption maximum of BZ–TCNE complex in the vapor phase.^{69,71}

For the C_{2v} geometry, the transition from the ground state to the lower-energy CT state (CT1) is forbidden by symmetry, whereas the transition to the higher-energy CT state (CT2) carries most of the oscillator strength. This is true for both X and Y conformers. However, because of the very floppy nature of the BZ–TCNE complex, facile large-amplitude intermolecular motions at room temperature should allow the CT1 state to gain a substantial excitation probability. Emery et al.^{55,92} have

Table 4. Calculated Energies, Oscillator Strengths, Interplanar Distances, and Dipole Moments of BZ–TCNE Complex

| optimized structure ^a | ground state ^b | | | excited states ^c | | | | | |
|----------------------------------|---------------------------|-----------------|-------------|-----------------------------|--------|-------|------|-----------------------|--------|
| | ΔE^b (eV) | R_{DA}^c (nm) | μ^d (D) | CT1 | | CT2 | | ΔE_{exp} (eV) | |
| Y conformer | 0 | 0.3016 | 1.80 | 4.268 | 0 | | 11.8 | 4.377 | 0.0963 |
| X conformer | 0.0017 | 0.3021 | 1.78 | 4.267 | 0 | | 11.9 | 4.378 | 0.0947 |
| CT1 _{min} //M06HF | 1.563 | | 1.64 | 3.371 (1.808) | 0.0107 | ~0.26 | 8.1 | 4.961 | 0.0516 |
| CT1 _{min} //CIS | 0.705 | | 0.93 | 3.598 (2.893) | 0.0124 | ~0.30 | 10.6 | 4.533 | 0.0230 |

^aY and X conformers are ground-state optimized structures at the M06HF/cc-pVTZ level of theory. CT1_{min}//M06HF and CT1_{min}//CIS are the first excited state optimized structures at the TD-M06HF//6-31G(d) and CIS//6-31G(d) levels of theory, respectively. ^b ΔE is the relative energy with respect to the Y conformer ground state. ^cAverage interplanar distances. ^dDipole moments. ^eOscillator strengths. ^fVapor-phase absorption maxima from ref 69. ^gPeak energy of the steady-state emission spectrum in CHX (this work).

found that the oscillator strengths from the ground state to the two CT states are sensitive functions of the ground-state structures on the basis of semiempirical calculations.^{55,92} Our calculations also showed that at some less symmetric structures the oscillator strengths of the CT1 and CT2 excitations can become comparable. CT1 excitation can also gain substantial intensity through vibronic coupling when proper vibrations are excited.⁹³ The distorted equilibrium structures predicted for the CT1 state (see below) should help to make the CT1 excitation vibronically allowed. Owing to the very small energy difference compared with the entire absorption bandwidth, state-selected excitation is not possible. The above considerations led to a conclusion that excitation near the maximum of the CT band probably excites both CT1 and CT2 states. For initial excitation to the CT2 state, a rapid CT2 → CT1 internal conversion can be expected because of the facile symmetry-breaking intermolecular motions and the very small energy gap.^{30,64,93} The possibility of such nonradiative transition has been predicted by Hayashi et al.^{30,64}

3.6.3. Optimized CT-State Structures. The CT1-state structure was optimized with a smaller basis set at the TD-M06HF/6-31G(d) and CIS/6-31G(d) levels of theory. The structure optimized at the former level is shown in Figure 12A.

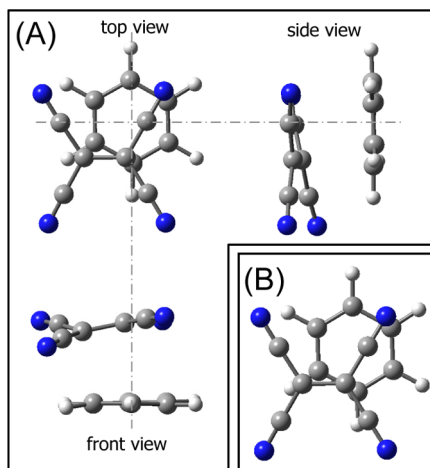


Figure 12. (A) Three views of the optimized CT1 excited-state structure of the BZ-TCNE complex at the TD-M06H/6-31G(d) level of theory. (B) Top view of the optimized CT1 excited-state structure of the BZ-TCNE complex at the CIS/6-31G(d) level of theory. The main difference between these two structures is that the average interplanar distance is shorter in the one optimized at CIS/6-31G(d).

The CT1-state equilibrium structure is predicted to be distorted from the C_{2v} symmetry with the TCNE significantly shifted away from the benzene center of symmetry. Similar laterally shifted structures have been predicted for BZ-TCNE by Emery et al. with semiempirical calculations.⁹² The vibrational frequencies calculated at these optimized structures (see the Supporting Information) gave no imaginary frequency, indicating that it corresponds to the true minimum at this level of theory. On the other hand, optimizations under the C_{2v} symmetry constraints yielded structures with more than one imaginary frequency. As shown in Figure 12A, the optimized CT1-state structure also suffers from internal structural distortions on both moieties in addition to the lateral shift. TCNE anion undergoes a substantial twist around the C=C double bond. The average separation between the two moieties also decreases to ~ 0.27 nm. This is not surprising because of

the strong Coulombic attraction between the two ions and is also consistent with the increase in intermolecular D-A stretching frequency from 96 cm^{-1} in the ground state to 194 cm^{-1} in the CT1 state (see the Supporting Information). The structure optimized at the CIS level, displayed in Figure 12B, also shows a similar laterally shifted geometry but with a much longer average interplanar distance of ~ 0.3 nm.

Single-point calculations were then carried out at the M06HF/cc-pVTZ level for the two optimized CT1-state structures, and the results are also summarized in Table 4. The vertical transition energies from the CT1-state minimum to the ground state is predicted to be 1.8 (685 nm) and 2.89 eV (428 nm) for the M06HF- and CIS-optimized structures, respectively. The discrepancy in transition energies between these two structures arises mainly from the difference in the interplanar distances. The observed emission maximum of BZ-TCNE in CHX (~ 550 nm, 2.23 eV) is between the values calculated for the two structures. The CT1-state dipole moments at the optimized CT1-structures are predicted to be 8.1 and 10.6 D for the M06HF- and CIS-optimized structures, respectively. Again, the discrepancy is probably due to the difference in the interplanar distances. It is plausible that the dipole moment at the CT1-state equilibrium structure is somewhere between these two predicted values. Note that the calculations reported here did not include solvation, which can strongly affect the CT-state energetics and structures, especially in solvents of strong polarities.

Although more sophisticated methods are definitely needed for more accurate descriptions of the CT states, a qualitative picture that has emerged from our calculations is that the CT-state equilibrium structure is very different from that of the ground state. Thus, upon vertical excitation to the CT state, a structural relaxation from the initial FC configuration (C_{2v}) to the equilibrium structure (distorted) via vibrational relaxation should prevail.

4. DISCUSSION

4.1. Steady-State Absorption and Fluorescence Spectra. Table 1 lists the steady-state spectral characteristics of BZ-TCNE in the three solvents along with those of C153 for comparison. The Stokes shift ($\delta\nu$), which is calculated as the frequency difference between the maxima of the absorption and fluorescence spectra, is a measure of the transition-energy change due to displacements along vibrational and solvent coordinates. The change in Stokes shift in going from CCl_4 to CH_2Cl_2 for BZ-TCNE is much larger than that for C153, suggesting a much larger dipole moment change in BZ-TCNE upon excitation. The Stokes shift in CCl_4 is only about 800 cm^{-1} greater than that in CHX. Although both CCl_4 and CHX are nonpolar solvents, solvation in CCl_4 usually produces a small but nonnegligible contribution to the Stokes shift, probably as a result of the presence of four polar bonds.⁸⁹ On the other hand, CHX is usually considered as a solvent in which polar solvation is negligible,^{79,94–98} and therefore, the Stokes shift observed in CHX must arise from the intramolecular structural changes. The slightly larger Stokes shift observed in CCl_4 indeed indicates that the polar solvation in CCl_4 is small but not negligible.

The relatively large Stokes shift and the broad, unstructured absorption and fluorescence spectral profiles of BZ-TCNE in CHX indicate that the complex must undergo a significant structural change upon CT excitation with many FC active modes. Upon CT excitation, the complex is instantaneously

transformed from a neutral configuration ($D-A$) to an ionic form (D^+-A^-) with a high degree of CS. The equilibrium structures of the ions, D^+ and A^- , are expected to differ substantially from those of the neutral D and A along some internal coordinates. Indeed, resonance Raman studies of HMB-TCNE in CCl_4 have concluded that there are at least 11 strongly FC active modes.^{28,29} Moreover, our electronic structure calculations predicted that the $D-A$ intermolecular geometries also undergo a large change because of the very different natures of interactions between the ground and CT states. Accordingly, many low-frequency intermolecular $D-A$ modes are also expected to be FC-active. The steady-state spectral characteristics of BZ-TCNE in nonpolar solvents are very similar to those reported for HMB-TCNE in the same solvents,^{28,57,62} and for the latter case, it has been shown that a total of 33 vibrational modes must be included to simulate the experimentally observed absorption and fluorescence spectra.³⁰ Because polar solvation is negligible in CHX, the 0-0 transition frequency can be estimated from the crossing point of the reduced absorption and fluorescence spectra to be at $\sim 22300\text{ cm}^{-1}$. Accordingly, the initial vibrational energy deposited in the BZ-TCNE CT state at 383 nm excitation is $\sim 3800\text{ cm}^{-1}$.

Although the steady-state fluorescence of BZ-TCNE in CH_2Cl_2 peaks at $\sim 750\text{ nm}$, there is a substantial emission extending to the blue-green region, which is consistent with the observed temporal behaviors of the TRFL spectra. In CH_2Cl_2 , the equilibrium emission in the red spectral region lasts for a relatively short lifetime ($\sim 29\text{ ps}$), and therefore, the early time blue-green emission constitutes an important fraction of the steady-state spectrum. On the other hand, the fraction of the blue emission in the CCl_4 spectrum is much smaller because the equilibrium emission after spectral relaxation is much slower (150 ps).

4.2. Dynamic Stokes Shifts: Solvation vs Intramolecular Relaxation. As shown in Figures 2–5, rapid spectral relaxations of different magnitudes occur upon CT excitation of the BZ-TCNE complex in the three solvents. Such relaxations manifest the nonequilibrium responses of the solute–solvent system to perturbations caused by solute excitation and are best described by the time-dependent mean emission frequency, $\bar{\nu}(t)$, shown in Figure 7. Rapid spectral relaxation in dipolar solvents is associated mainly with polar solvation, but as has been discussed elsewhere, intramolecular relaxation dynamics can also contribute.^{99–104}

The data shown in Figure 7 were analyzed using the deconvolution procedure described above, and the results are summarized in Tables 1 and 2. The total dynamic Stokes shift, $\Delta\bar{\nu}_{0\infty} = \bar{\nu}(0) - \bar{\nu}(\infty)$,¹⁰⁵ amounts to 7300 cm^{-1} in CH_2Cl_2 . In the cases of CCl_4 and CHX, the total dynamic Stokes shifts reduce to about 3500 and 2500 cm^{-1} , respectively, much smaller than that observed in CH_2Cl_2 , but certainly not negligible. The deconvoluted mean emission frequencies near time zero ($\bar{\nu}(0)$) are 20300 and 20000 cm^{-1} for CH_2Cl_2 and CCl_4 , respectively. In the case of CHX being the solvent, the total dynamic Stokes shift cannot be accurately determined owing to the severe interference arising from the very intense Raman bands within the first picosecond.⁷⁸ However, the fact that $\bar{\nu}(0)$'s are at $\sim 20000\text{ cm}^{-1}$ in the two solvents (CH_2Cl_2 and CCl_4) of very different polarities suggests that $\bar{\nu}(0)$ for BZ-TCNE in CHX must also be close to 20000 cm^{-1} . This estimation gives a total dynamic Stokes shift of $\sim 2500\text{ cm}^{-1}$ for BZ-TCNE in CHX. This finding is quite surprising because CHX is not expected to produce any measurable TDFSS due to

solvation.^{79,94,95} Thus, the relatively large dynamic Stokes shift observed here in CHX must be due solely to intramolecular relaxation, which should also be present in other solvents, polar and nonpolar, with similar magnitudes. Accordingly, we conclude that the total dynamic Stokes shifts of 7300 and 3500 cm^{-1} measured for BZ-TCNE in CH_2Cl_2 and CCl_4 , respectively, also contain an intramolecular relaxation contribution of about 2500 cm^{-1} . The contributions of intramolecular relaxation, including electronic and vibrational, in the TDFSS measurements have been discussed in the literature.^{80,95,99–104} In the following, we discuss the possible intramolecular dynamics that can give rise to the observed TDFSS.

4.2.1. Intramolecular Electronic Transition: Evidence for the CT2 to CT1 Transition. In the present system, a possible rapid electronic relaxation that can take part in the observed spectral relaxation is the $CT2 \rightarrow CT1$ transition. As discussed earlier, under C_{2v} symmetry, the $CT1$ excitation in BZ-TCNE is forbidden, and the transition to the $CT2$ state carries most of the oscillator strength. However, the ground-state BZ-TCNE can undergo facile large-amplitude intermolecular motions at room temperature because of its very floppy nature, allowing the $CT1$ state to gain a substantial excitation probability. For those initially excited to the $CT2$ state, the subsequent $CT2 \rightarrow CT1$ transition is facile due to the constant symmetry-breaking motions and the small energy gap.^{30,64,93}

A spectral feature consistent with the $CT2 \rightarrow CT1$ transition is the fast decaying component appearing in the blue region ($<450\text{ nm}$) of the early time TRFL spectra in CH_2Cl_2 . This component exhibits spectral and temporal behaviors that are distinctive from the rest of the emission, that is, it decays rapidly but stays in the blue region with a much smaller dynamic Stokes shift. The fluorescence decay traces (see Figure 6A) within this blue spectral feature are close to the temporal IRF, and only a lifetime of $\tau \leq 0.1\text{ ps}$ can be concluded. Similar spectral features are also present in the early time TRFL spectra in CCl_4 but are less noticeable, probably because of the broader IRF (0.5 ps) used in this case. In the CHX case, this component was difficult to observe because the strong Raman bands overwhelmed the same temporal and spectral regions,⁷⁸ and the broader IRF (0.75 ps) used in this case made this component even less noticeable. A support to the $CT2 \rightarrow CT1$ assignment is that the total fluorescence intensity decay with cubic frequency correction, $P(t)$, which will be discussed in detail below, exhibits a fast initial decay component of similar time scales. Because the $CT2$ state lifetime is shorter than 0.1 ps , it experiences only limited polar solvation before converting into the $CT1$ state. Therefore, the emission appearing within the IRF does not show significant Stokes shifts. Once the $CT1$ state is reached, the small electronic energy difference of $\sim 900\text{ cm}^{-1}$ is converted to the vibrational energy of the $CT1$ state, which may appear in $CT1$ emission if IVR is not fast enough (see below). These considerations suggest that the fastest components identified in $\bar{\nu}(t)$ of all three solvents may contain a small contribution ($<900\text{ cm}^{-1}$) due to the $CT2 \rightarrow CT1$ transition.

4.2.2. Vibrational Relaxation. As discussed above, the $CT2 \rightarrow CT1$ electronic transition alone cannot account for the total of 2500 cm^{-1} of intramolecular contributions in the observed TDFSS. Hence, the major portion of the intramolecular dynamic Stokes shift must be due to vibrational relaxation, which includes IVR and VC. The latter process is the dissipation of solute vibrational energy via collisional energy

transfer to achieve a thermal equilibrium with the surrounding solvents. We assert that vibrational relaxation can contribute to the observed TDFSS if IVR is slow compared with the time resolution of the experiment. Here, we discuss the effect of different IVR time scales regarding the observed TDFSS by considering two limiting cases.

The first case is when IVR is much slower than the time resolution. In such a case, spectral evolutions due to IVR should appear in the TRFL spectra. Vertical excitation of large polyatomic molecules usually deposits a substantial amount of vibrational energy in some FC active modes. Before this energy relaxes out of these FC modes, the TRFL spectra are expected to differ from those observed after the completion of IVR.^{59,94,95,100,106,107} Specifically, the early time spectra should contain higher-frequency emission originating from high vibrational levels in the excited state to low vibrational levels in the ground state ($\nu' > \nu''$) in FC modes.^{58,59} Maroncelli's group⁹⁴ has pointed out that it is incorrect to determine the solvation response function using the true time-zero spectrum as a measure of $\bar{\nu}(0)$ because the TDFSS thus defined may contain contributions from IVR. Consequently, they have used a special approach to determine the "time-zero" spectrum by comparing with the steady-state spectrum measured in a reference nonpolar solvent.^{79,94} The fluorescence spectral profiles of large polyatomic molecules are usually dominated by the vibronic structures of high-frequency FC modes. Once IVR completes, the excess vibrational energy is equilibrated among the intramolecular modes, and the average excitations in high-frequency FC modes become very low. The observed TRFL spectral profiles are then predominated by vibronic transitions originating from the zero vibrational level in high-frequency FC modes, while excitations in low-frequency modes simply make these major vibronic features broad and less structured. The fluorescence spectra observed shortly after excitation (a few picoseconds) in the gas phase implemented by the "chemical timing" technique clearly revealed such spectral evolutions.^{108–110} The subsequent energy dissipation into the solvent through VC merely causes band narrowing^{41,81,111} with a negligible Stokes shift. However, if the IVR rate is comparable to or slower than VC, the latter can also result in observable TDFSS. Thus, in this slow IVR case, vibrational relaxation (IVR, VC, or both) can result in observable TDFSS.

In the other extreme case, IVR is much faster than the time resolution such that the observed TRFL spectra near the time zero within the detection time window are dominated by emissions after the completion of IVR. In such a case, early spectral evolutions due to IVR are smeared out,¹¹² and IVR contributes negligibly to the measured TDFSS. Most solvation probes, including C153, belong to this case because they are usually large organic dye molecules in which IVR often occurs much faster than 0.1 ps in solutions. Again, the subsequent slower energy dissipation into the solvent (VC) only causes band narrowing^{41,81,111} with negligible Stokes shifts. Thus, in this extremely rapid IVR case, vibrational relaxation does not contribute to the observed TDFSS, and the spectral dynamics provides a true measure of the solvation response.

The latter case is demonstrated in our own TDFSS measurements of C153 in CH_2Cl_2 solution (Figure 10A), in which two fast spectral relaxation components, $\tau_1 = 0.20 \pm 0.05$ ps and $\tau_2 = 1.0 \pm 0.1$ ps, were identified (Figure 10C). These values are consistent with the CH_2Cl_2 solvation times (0.144 and 1.02 ps) reported by the Maroncelli's group, who also used C153 as the probe.⁷⁹ Excitation of C153 in CH_2Cl_2 at 383 nm

deposits $\sim 3900 \text{ cm}^{-1}$ of vibrational energy in the S_1 state,¹¹³ and therefore, VC must proceed after the completion of rapid IVR to dissipate this excess energy into the solvent. However, the observed relaxation in TDFSS (<1 ps) is much faster than what would be expected for VC in typical organic solvents, which should be on the order of at least a few picoseconds.^{35,36,40,41} Therefore, VC of more than 0.5 eV of vibrational energy does not produce observable contributions in the TDFSS of C153 in CH_2Cl_2 . The reason is simply that IVR in C153 is, indeed, much faster than the present time resolution (0.35 ps). On the other hand, the time dependence of the TRFL bandwidth (Figure 10D) exhibits, in addition to the two ultrafast solvation components, a slow component of ~ 10 ps that is consistent with VC.

For the BZ–TCNE system, we have concluded that a major portion of the intramolecular contribution ($\sim 2500 \text{ cm}^{-1}$) in the observed TDFSS is due to vibrational relaxation. This conclusion, when combined with the above discussions, surprisingly suggests that the IVR time scales in BZ–TCNE are comparable to or even slower than our time resolutions (0.35–0.75 ps). The present system, BZ–TCNE, is indeed very unique with regard to IVR. Overall, the BZ–TCNE complex is a relatively large system with 22 atoms in total. However, the couplings between the vibrational modes localized in BZ and TCNE moieties are rather weak, and therefore, the vibrational energy tends to randomized first within the BZ and TCNE moieties before a global equilibrium is reached. Thus, BZ–TCNE may behave more like an intermediate-sized system as far as IVR is concerned. Recent ultrafast time-resolved studies of systems with similar molecular sizes and excitations in solutions indeed reveal IVR time scales ranging from subpicoseconds (>0.1 ps) to a few picoseconds.^{31–36} Moreover, the intermolecular modes between BZ and TCNE, which are expected to be highly FC-active, are also very weakly coupled to internal modes in both moieties. These unique properties of the BZ–TCNE complex suggest the presence of nonstatistical and slow IVR that can make vibrational relaxation observable in the TDFSS measurements. Interestingly, a recent report¹¹⁴ has shown that hindered IVR can, indeed, lead to nonergodic behaviors in medium-sized ion pairs in which the noncovalent nature of the bonding appears important.

4.3. TDFSS in CHX: IVR and VC Dynamics. Analyses of $\bar{\nu}(t)$ show that there are at least three spectral relaxation components for BZ–TCNE in CH_2Cl_2 and CCl_4 (see Table 2 and Figure 7). In the case of CHX, because $\bar{\nu}(t)$ data before 1 ps are not available, only a slow component of ~ 11 ps responsible for $\sim 1000 \text{ cm}^{-1}$ of TDFSS can be identified. However, as discussed earlier, $\bar{\nu}(0)$ in CHX is expected to be close to 20000 cm^{-1} , and therefore, the fact that $\bar{\nu}(1 \text{ ps}) \sim 18500 \text{ cm}^{-1}$ suggests that a subpicoseconds relaxation responsible for about 1500 cm^{-1} of TDFSS must also exist. In addition to a small possible contribution ($<900 \text{ cm}^{-1}$) due to the $\text{CT2} \rightarrow \text{CT1}$ transition, the rest of the TDFSS relaxation observed in CHX can be assigned to vibrational relaxation due to slow IVR. These reasonings suggest that the vibrational relaxation contribution in the observed TDFSS is at least biphasic in CHX, i.e., a fast subpicoseconds component followed by a much slower one of about 11 ps. Similar biphasic behaviors of vibrational relaxation must also exist in the other two solvents. Therefore, the slowest component observed in CH_2Cl_2 and CCl_4 can also be assigned to vibrational relaxation, consistent with the conclusion drawn on the basis of solvation considerations, as discussed below.

The biphasic vibrational relaxation contribution in TDFSS cannot be simply due to a rapid IVR completed in less than a picosecond followed by a slower VC because in such cases, VC gives rise only to band narrowing with negligible TDFSS, as demonstrated in the C153 case discussed above. We propose that the slow and biphasic vibrational contributions observed in TDFSS are due to nonstatistical IVR in the BZ–TCNE complex. Recent experimental and theoretical studies have concluded that IVR in solutions is still dictated by specific low-order resonances and can be nonstatistical even for large systems at high levels of excitation.^{31–36,115,116} For example, femtosecond IR pump/UV probe experiments reported by the Abel's group^{117,118} have shown that for intermediate-sized systems, such as benzene and toluene, in solutions, the IVR takes place in two sequential steps of very different time scales: an ultrafast initial step of <0.5 ps (limited by their time resolution) and a second much slower one of a few picoseconds. Such biphasic behaviors in IVR can be well understood with the tier model.^{32,33,116–118} The initial rapid IVR corresponds to the relaxation of the initially excited state to the strongly coupled first tier levels, whereas the second slower steps are due to the subsequent relaxation to less-coupled levels of higher tiers. Similar sequential IVR processes may occur in the present system and are responsible for the relaxation within the first few picoseconds.

Another possible cause of the biphasic vibrational contribution in the observed TDFSS is the nonuniform initial phase-space distribution in combination with some localization effects^{119–121} (IVR bottlenecks) that restrict the vibrational-energy flow in molecules. Excitations in some low-frequency FC modes may play an important role in this case. Our calculations predicted that there are 11 vibrational modes with frequencies below 200 cm⁻¹ in the BZ–TCNE CT excited states (see the Supporting Information). Moderate excitations in these low-frequency modes cannot access the high-frequency ones in both moieties because of energetic and coupling reasons. Two types of vibrational modes can be considered for this mechanism. The first one is the low-frequency modes localized in either the BZ⁺ or TCNE⁻ moiety. One good candidate is the TCNE out-of-plane bend responsible for the coherent vibration observed by Rubtsov and Yoshihara^{58,59} in the HMB–TCNE complex. This mode can be highly excited upon CT excitation due to the out-of-plane deformation of TCNE anion in the complex. Being a low-frequency out-of-plane mode, it is expected to be only weakly coupled to a few other low-frequency modes in TCNE. Indeed, the vibrational coherence, which is more relevant to vibrational wave packet dephasing, observed in HMB–TCNE lasts for about a picosecond.^{58,59} Thus, relaxation in the TCNE anion out-of-plane bending mode may account for the observed TDFSS relaxation on subpicosecond time scales.

The other types of modes that may be involved in the slow IVR are the D–A intermolecular vibrations. As shown in Figure 12, our calculations predicted that the CT-state equilibrium structure is quite different from that of the ground state. Consequently, nearly all D–A intermolecular modes are expected to be FC-active and are highly excited upon CT excitation. Vibrational energies deposited in these D–A intermolecular modes may redistribute among themselves, but because the couplings to higher-frequency intramolecular modes in either D⁺ or A⁻ are rather weak, they can be trapped within these intermolecular modes for a long time. Concurrently, VC can dissipate the intermolecular vibrational

energy into the solvent before global IVR completes. In this case, the observed spectral relaxation simply reflects the VC dynamics. The slowest components observed in all three solvents are, indeed, consistent with VC time scales in simple aprotic solvents.^{35–41} Once the energy localized in the intermolecular modes is dissipated into the solvent, the complex is stabilized into the CT-state equilibrium structure. Such a relaxation process is, in fact, equivalent to the structural relaxation from the FC configuration to the equilibrium structure of the CT state. The key for the slow VC process to be observed here in the TDFSS is the hindered IVR that traps vibrational energy in a few intermolecular FC-active modes. The dissipation of energy (VC) localized in these modes then gives rise to the slow red shift in emission frequency.

Our assignment of the slowest relaxation component to slow vibrational relaxation, that is, slow IVR followed by VC, should be compared with the intracomplex structural relaxation proposed by the Mataga's group.^{122–125} In their early femtosecond–picosecond transient absorption studies of EDA complexes of 1,2,4,5-tetracyanobenzene (TCNB) with a series of MBZs in acetonitrile, they concluded that the photoinduced CS takes place in two distinctive steps: a very fast one (<1 ps) due to solvation and a slower one with time constants ranging from a few to a few tens of picoseconds that can be ascribed to an intracomplex structural relaxation. Judging from the similarity in time scales, we believe that the slow relaxation components observed in both systems are of the same origin. The intracomplex structural relaxation they described is equivalent to the slow vibrational relaxation discussed here. Indeed, the time scales they reported for the intracomplex structural relaxation of MBZ–TCNB do suggest the presence of hindered IVR in the intermolecular vibrational modes.

4.4. TDFSS in CH₂Cl₂ and CCl₄: Solvation and Vibrational Relaxation Dynamics. Figure 7A shows the observed $\bar{\nu}(t)$ upon CT excitation of BZ–TCNE in CH₂Cl₂. The total dynamic Stokes shift measured in CH₂Cl₂ (7300 cm⁻¹) is much larger than those observed in nonpolar solvents, indicating a significant polar solvation in response to dipole moment change. Three temporal components were identified: $\tau_1 = 0.2$ ps, $\tau_2 = 0.8$ ps, and $\tau_3 = 15$ ps. The time scales of the first two fast components are similar to the solvation times of CH₂Cl₂ reported by the Maroncelli's group (0.144, 1.02 ps)⁷⁹ and in this work ($\tau_1 = 0.2$ ps; $\tau_2 = 1.0$ ps). Accordingly, it is reasonable to assume that a major portion, but not all, of these two faster components observed in CH₂Cl₂ (τ_1 and τ_2) is due to the rapid solvation. The first two components account for about 5750 cm⁻¹ of TDFSS in CH₂Cl₂, and the subpicosecond component in CHX due to intramolecular relaxation is responsible for only ~1500 cm⁻¹. A similar subpicosecond intramolecular contribution is expected to be also present in CH₂Cl₂, suggesting that the polar-solvation contribution to TDFSS in CH₂Cl₂ is ~4250 cm⁻¹.

Comparing with the C153 data, it is evident that the slowest relaxation component of 15 ps observed in $\bar{\nu}(t)$ cannot be due to pure solvation because its time scale is much longer than the expected solvation time scales in CH₂Cl₂. Therefore, it must originate from some intramolecular relaxation dynamics that are unique to the solute. This conclusion is in line with that reached above on the basis of the biphasic TDFSS relaxation in CHX, and we have proposed that the slowest component observed in TDFSS is mostly due to the slow relaxation of the D–A intermolecular vibrations, which is equivalent to the

structural relaxation from the FC configuration to the equilibrium CT-state structure. The magnitude of the slowest component in CH_2Cl_2 ($\sim 1550 \text{ cm}^{-1}$) is substantially larger than that in CHX ($\sim 1000 \text{ cm}^{-1}$), implying other contributions to the TDFSS may be present in polar solvents.

In the case of CCl_4 being the solvent, the total dynamic Stokes shift amounts to $\sim 3500 \text{ cm}^{-1}$, much smaller than that observed in CH_2Cl_2 . As indicated in Figure 7B, three temporal components were also identified in $\bar{\nu}(t)$: $\tau_1 = 0.4 \text{ ps}$, $\tau_2 = 0.9 \text{ ps}$, and $\tau_3 = 14 \text{ ps}$. Probably because of the very small dynamic Stoke shift, to the best of our knowledge, no TDFSS measurements in CCl_4 have been reported. However, Larsen et al.¹²⁶ have measured the solvation dynamics of a quadrupolar solute in CCl_4 using the three-photon echo peak shift technique. Their data revealed three solvent dynamical time scales for CCl_4 : a 80 fs ultrafast component attributed to inertial motions and another two slower components of 0.5 and 2.0 ps.¹²⁶ We have made an attempt to measure the TDFSS of C153 in CCl_4 with the present setup. As shown in Figure 10B, TRFL spectra measured for C153 in CCl_4 exhibit very little spectral relaxation. The total dynamic Stokes shift is $< 300 \text{ cm}^{-1}$, consistent with the value reported by Reynolds et al.⁸⁹ Because of the very small dynamic Stokes shift and the poor quality of the data,¹²⁷ we could only conclude that the solvation time scale is no greater than 1.5 ps. It is likely that multiple components are present but cannot be resolved in this case. On the basis of these solvation data, the two faster relaxation components (0.4 and 0.9 ps) observed in the BZ–TCNE/ CCl_4 TDFSS data can be attributed, at least in part, to rapid solvation because their time scales are similar to the expected solvation times of CCl_4 . The 0.4 ps component is probably an unresolved combination of the 80 fs and 0.5 ps components reported by Larsen et al.¹²⁶ Again, the slowest component of $\sim 14 \text{ ps}$ cannot be due to solvation because its time scale is much longer than the solvation times in CCl_4 and must be assigned to vibrational relaxation, as in the case of CHX and CH_2Cl_2 .

The magnitude of TDFSS of the slowest component in CCl_4 (1200 cm^{-1}) is slightly larger than that in CHX ($\sim 1000 \text{ cm}^{-1}$) but is smaller than that in CH_2Cl_2 . The first two components account for about 2300 cm^{-1} of TDFSS. Subtracting the subpicosecond intramolecular contribution (1500 cm^{-1}) estimated from the CHX data, we concluded that the solvation contribution to TDFSS in the BZ–TCNE/ CCl_4 system is only $\sim 800 \text{ cm}^{-1}$. Rubtsov and Yoshihara^{58,59} have attributed both spectral relaxation components (0.115 and 1.4 ps) of $\sim 1200 \text{ cm}^{-1}$ they measured following CT excitation of HMB–TCNE in CCl_4 to vibrational relaxation only. It is our opinion that both solvation and vibrational relaxation are involved in the fast spectral relaxation they observed. Because the data they reported were only up to about 1.2 ps,^{58,59} it is not clear if a third slower component is also present in the HMB–TCNE system.

The change of the solvation contribution in TDFSS of BZ–TCNE in going from CCl_4 ($\sim 800 \text{ cm}^{-1}$) to CH_2Cl_2 ($\sim 4250 \text{ cm}^{-1}$) is $\sim 3450 \text{ cm}^{-1}$, whereas the corresponding change for C153 is only $\sim 800 \text{ cm}^{-1}$. This comparison suggests that the dipole moment change upon CT excitation in BZ–TCNE is much greater than that in C153.

4.5. Time Dependence of TRFL Spectral Bandwidths.

The temporal dependence of the spectral bandwidth is also an important characteristic of TRFL spectra that can be associated with solvation⁷⁹ and vibrational relaxation.^{81,82,100,128} The solvation contribution to the band sharpening is mainly due

to the narrowing of the solvent structure distribution.⁷⁶ Figure 8 shows the time-dependent bandwidth, $W(t)$, of TRFL spectra of BZ–TCNE in the three solvents studied here. In the case of CH_2Cl_2 , the initial TRFL spectra near time-zero exhibit extremely large bandwidths of more than 10000 cm^{-1} ; they then sharpen rapidly and gradually relax to less than 4000 cm^{-1} at long times. Similar behaviors are also observed in the CCl_4 case. These data were analyzed by simply fitting $W(t)$ with a multiexponential model function convoluted with the IRF. In both CH_2Cl_2 and CCl_4 , three temporal components were identified, and the results are summarized in Table 3. Because data before 1 ps are not available in the CHX case, only a fast component of $\sim 1 \text{ ps}$ and a slow component of about 13 ps were identified. It is likely that an unresolved subpicosecond component is also present in the CHX data.

Because polar solvation is not expected in CHX, the biphasic bandwidth relaxations of relatively small magnitudes in CHX must be due to vibrational relaxation. On the other hand, the time scales and magnitudes of the two fast components identified in CH_2Cl_2 and CCl_4 suggest that they are mostly due to solvation, whereas the third slowest components are most likely due to vibrational relaxation. The time constants derived from the time-dependent bandwidth data are consistent with, but not identical to, those derived from the TDFSS measurements, probably because each spectral property may exhibit distinct time dependence.

Either complete or incomplete IVR produces a quasiequilibrium distribution in the vibrational manifold equivalent to an elevated temperature of the ensemble, making the TRFL spectra broad and less structured. Thus, IVR should result in an initial broadening, which was not clearly observed here, probably because of the overwhelming solvation band narrowing. When the vibrational energy is dissipated into the solvent via VC, the excited state is thermally equilibrated with the solvent, and the TRFL spectra become narrower. However, because fluorescence spectral profiles of large molecules are usually dominated by the vibronic structures of a few high-frequency FC modes, the broadening of the thermally unrelaxed ensemble after IVR is not significant compared with the entire bandwidth. The C153 data shown in Figure 10 manifest this effect. Excitation of C153 in CH_2Cl_2 at 383 nm deposits $\sim 3900 \text{ cm}^{-1}$ of vibrational energy in the excited state,¹¹³ and yet, the VC component in the $W(t)$ derived from C153 data is responsible for only about 300 cm^{-1} of band narrowing. This explains the relatively small magnitude of the slowest component in all $W(t)$ data of the BZ–TCNE. The process responsible for the majority of band narrowing is solvation.

4.6. Total Fluorescence Decay and Equilibrium Charge Recombination Dynamics. The spectral relaxation components identified in $\bar{\nu}(t)$ and $W(t)$ are entangled with other dynamical processes in the fluorescence transients shown in Figure 6 at various wavelengths, making it difficult to separate one from the others. On the other hand, the total fluorescence intensity with cubic-frequency correction, $P(t)$, of eq 3 provides a more direct measure of the excited-state population decay. To a good approximation, $P(t)$ represents the temporal dependence of the product of the excited-state population, $N(t)$, and the square of the mean emission electronic transition moment, $\bar{M}_{\text{em}}(t)$, that is, $P(t) \propto N(t) \cdot \bar{M}_{\text{em}}^2(t)$.^{25,59,83} Temporal components due to pure spectral relaxation processes that do not alter excited-state total populations, for example, solvation and vibrational relaxation,

are expected to be greatly suppressed in this function. This is demonstrated in Figure 10E and F with the $P(t)$ and $J(t)$ obtained from the same C153 TRFL spectra in CH_2Cl_2 . $J(t)$ contains a small initial decay due to solvation, whereas the $P(t)$ exhibits a nearly constant intensity, indicating that the excited-state population and emission transition moment do not change noticeably within the first 10 ps. For emission originating from a single excited state with a rigid molecular structure, $\bar{M}_{\text{em}}(t)$ is approximately constant with time. In the present case, both CR rate and the emission transition moment are sensitive functions of the BZ–TCNE structure and may evolve with time during the relaxation.

Figure 9 shows the $P(t)$ derived from the TRFL spectra of BZ–TCNE in the three solvents. These data were fit with multiexponential functions convoluted with the IRF, and the results are also summarized in Table 3. In CH_2Cl_2 , a very rapid initial decay (<0.1 ps) was clearly identified. A similar rapid component is also present in the CCl_4 $P(t)$, but is less noticeable, probably because of the broader IRF. Because the excited-state population decays in a much longer time scale (see below), this ultrafast decay component must be due to a rapid change in emission transition moment following the initial excitation. We assigned this initial fast decay to the rapid $\text{CT}2 \rightarrow \text{CT}1$ transition. As discussed earlier, the oscillator strength for the $\text{CT}2$ emission in the FC region is relatively large, whereas that in the $\text{CT}1$ state is lower, even at the non- C_{2v} equilibrium structure (see Table 4). Thus, for those initially excited to the $\text{CT}2$ state, the subsequent rapid $\text{CT}2 \rightarrow \text{CT}1$ transition should result in a sudden emission intensity reduction in <0.1 ps. It should be noted that the relative amplitude of this initial rapid decay with respect to other slower components is, in fact, much larger than it appears because of the effect of convolution with broad IRFs. Other ultrafast processes, such as initial wave packet motion and solvation-induced charge separation, may also contribute to this rapid component and cannot be completely ruled out.

Apart from the initial rapid decay, the $P(t)$ functions exhibit temporal profiles that are strongly solvent-dependent. The $P(t)$ derived from the TRFL spectra in CH_2Cl_2 exhibits a pronounced biexponential decay composed of a faster component of ~3.2 ps, followed by a slower one of 29 ps. On the other hand, The $P(t)$ s derived from TRFL spectra in CCl_4 and CHX are dominated by single exponential decay of 150 and 70 ps, respectively. This marked difference in the temporal dependence of total fluorescence intensity is recognizable even in the TRFL spectra presented in Figures 2–4 and the transients shown in Figure 6. Another less noticeable difference is that the $P(t)$ obtained from the CCl_4 data initially remains nearly constant for a period of about 10 ps, which is then followed by an exponential decay of ~150 ps. Similar behaviors seem to be also present with a shorter time scale in the CHX $P(t)$ profile. Unfortunately, because the data before 1 ps are not available for CHX, it is difficult to come to a certain conclusion. These general observations suggest that the CT-state decays are nonexponential and that nonequilibrium CR may be involved. In the following, we will first discuss the equilibrium CR dynamics manifested by the slowest component in $P(t)$ before addressing the nonexponential temporal behaviors.

The time constants of the slowest components observed in $P(t)$ s are 29 ps in CH_2Cl_2 , 150 ps in CCl_4 , and 68 ps in CHX. Because these much slower components do not appear in the temporal dependence of spectral properties ($\bar{v}(t)$ and $W(t)$),

they are definitely not associated with any spectral relaxation processes. Accordingly, these components can be safely ascribed to the population decay of the equilibrium CT state following all preceding relaxation processes along solvent and internal coordinates. The fully solvated equilibrium CT excited state of an EDA complex is equivalent to the so-called “contact ion pair” and can undergo either CR or dissociation into free ions, both of which lead to CT-state population decay. However, dissociations of CIPs into free ions are known to take a much longer time scale,^{9,10,60,129–131} and therefore, the 30–150 ps components observed here must be due to CR.

One important parameter pertaining to the CR rate is the reaction exothermicity ($-\Delta G^0$), or the driving force, which can be estimated from the absorption and fluorescence spectra. Assuming identical energy profiles for the ground and excited states along solvation and internal coordinates, the total reorganization energy can be approximated by $\lambda \approx (\hbar\nu_{\text{abs}}^{\text{max}} - \hbar\nu_{\text{em}}^{\text{max}}(\infty))/2$,^{130,132,133} where $\nu_{\text{abs}}^{\text{max}}$ is the frequency at absorption maximum and $\nu_{\text{em}}^{\text{max}}(\infty)$ is the frequency at emission maximum at infinite time where solvation and vibrational relaxation have completed. The latter was taken as the peak position of the TRFL spectra at long delay times. The driving force ($-\Delta G^0$) for the CR reaction is then given by $-\Delta G^0 \approx \hbar\nu_{\text{abs}}^{\text{max}} - \lambda$. Table 5 gives the estimated λ and $-\Delta G^0$ values using these approximations along with the observed equilibrium CR time constants.

Table 5. Estimated Reorganization Energies and Reaction Exothermicities, And Experimental Equilibrium CR Time Constants

| | λ^a (eV) | $-\Delta G^{0a}$ (eV) | τ_{CR}^b (ps) |
|--------------------------|------------------|-----------------------|---------------------------|
| CH_2Cl_2 | 0.787 | 2.40 | 29 |
| CCl_4 | 0.570 | 2.61 | 150 |
| CHX | 0.515 | 2.68 | 68 |

^a λ and $-\Delta G^0$ are reorganization energies and reaction exothermicities estimated with the observed spectroscopic parameters, respectively.

^bExperimentally determined CR time constants.

The equilibrium CR rate of the BZ–TCNE CT state in CH_2Cl_2 is much faster than those in CCl_4 and CHX. In CH_2Cl_2 , strong polar solvation greatly decreases the free energy of the equilibrium CT state, making the driving force for CR in CH_2Cl_2 at least 0.2 eV lower than those in the other two nonpolar solvents. Thus, CR proceeds at a higher rate in CH_2Cl_2 , as expected for the “inverted region,” in which the logarithm of the CR rate constant has been shown to decrease linearly with increasing reaction exothermicity.^{10,134,135} However, a reversed trend is observed between CCl_4 and CHX. The driving force estimated for CR in CCl_4 is ~0.07 eV lower than that in CHX, and yet, the CR rate observed in CHX is faster by a factor of ~2. Because the energy factor alone predicts the opposite trend, this anomalous solvent effect must be due to some subtle variation of electronic coupling in different solvents.

These equilibrium CR rates should be compared with those reported previously for similar systems. To the best of our knowledge, the only time-resolved spectroscopic data of BZ–TCNE in the literature is a transient-absorption study which reported a CR rate of $1.4 \times 10^{10} \text{ s}^{-1}$ ($\tau_{\text{CR}} = 71 \text{ ps}$) in CH_2Cl_2 .⁷² This is more than a factor of 2 slower than the value determined in this work with TRFL spectroscopy; the origin of this disagreement is not clear at this point. Because benzene is a

weaker electron donor than any other methylbenzenes, it can be expected that CR rates of other MBZ–TCNE complexes in the same solvent should be higher because of the smaller driving force. For example, Wynne and Hochstrasser⁵⁷ reported a CR time constant of 16 ps for HMB–TCNE in CCl_4 , and Nicolet et al.⁴² reported subpicosecond CR times for TCNE complexes with isodurene (IDU), pentamethylbenzene (PMB), and HMB in acetonitrile. Jarzeba et al.⁵⁴ measured CR rates of toluene (TL)–TCNE complex in a series of solvents using femtosecond pump–probe transient absorption spectroscopy. The results relevant to the present study are $\tau_{\text{CR}}(\text{CH}_2\text{Cl}_2) = 8.5$ ps, $\tau_{\text{CR}}(\text{CCl}_4) = 400$ ps, and $\tau_{\text{CR}}(\text{CHX}) = 600$ ps. In CH_2Cl_2 , the CR rate of TL–TCNE is greater than that of BZ–TCNE, as expected. However, in both CCl_4 and CHX, the CR rates of TL–TCNE are lower than that of BZ–TCNE reported in this work. The exact cause of this anomalous behavior is not clear, but may be related to the higher symmetry and the absence of methyl-group hindrance in benzene.

4.7. Reaction-Field-Induced Structural Relaxation. As mentioned earlier, the temporal behavior of $P(t)$ is solvent-polarity-dependent. In CH_2Cl_2 , the $P(t)$ exhibits a conspicuous biexponential decay with a faster 3.2 ps component, followed by the slower equilibrium CR component of 29 ps. On the other hand, the $P(t)$ s derived from TRFL spectra in nonpolar solvents are dominated by slow, single exponential decays. The marked difference in the decay profiles of BZ–TCNE in CH_2Cl_2 and CCl_4 provides important implications on the CR dynamics. At first glance, the biexponential decay observed in CH_2Cl_2 could be an indication of vibrational nonequilibrium CR because the 3.2 ps decay is close to the general time scales of vibrational/structural relaxation; however, vibrational/structural relaxation also occurs in CCl_4 and CHX at similar time scales, and therefore, the lack of biexponential decay in the two nonpolar solvents immediately dismisses this speculation.

Biexponential decays of EDA complexes upon CT excitation have been reported previously, and a couple of possible mechanisms have been given to account for the observations.^{136–138} For example, Arnold et al.^{136,137} have reported biexponential CT-emission decays of EDA complexes with relatively long CT-state lifetimes in polar solvents and attributed their observations to the interconversion between the CIP and the solvent-separated ion pair (SSIP).^{136,137} The latter species is expected to be nonemitting, and the biexponential decay arises from the equilibrium kinetics. However, the time scale for the CIP and SSIP conversion is usually on the time scale of a few hundred picoseconds, even in high-polarity solvents,^{136,137} and therefore, the faster component of about 3 ps observed here in CH_2Cl_2 cannot be due to CIP/SSIP conversion.

Recently, Mohammed and Vauthey¹³⁸ reported biexponential transient-absorption decays of the methylperylene–TCNE complex in several polar solvents. They proposed that the two components are due to parallel excitations of two different complex geometries in the ground state.¹³⁸ Supported by some experimental evidence, they further proposed that the slower component arises from excitation of the “random DA pairs”^{60,129} that have a relatively large center-to-center distance and, thus, weaker electronic coupling and CT absorption.¹³⁸ However, this parallel excitation mechanism cannot account for the observations in this work. If the biexponential decay observed in CH_2Cl_2 were due to the parallel excitation of different complex geometries, similar behaviors would also be observed in nonpolar solvents. Moreover, it is difficult for the

extremely low concentration^{60,129} and weak CT transition moment of random DA pairs to justify the magnitude of the slow component observed in our case.

Because the biexponential decay is observed only in CH_2Cl_2 , we conceived that it must be due to a polarity-dependent mechanism that is present only in polar solvents but is greatly suppressed in nonpolar solvents. In solvents of high polarity, an additional structural relaxation involving both solvent and vibrational coordinates may become operative. Upon CT excitation, the BZ–TCNE complex is prepared in its FC state with an instantaneous and large dipole moment change, inducing a rapid solvation that occurs in less than a picosecond in simple aprotic dipolar solvents. The polarized solvation shell produces a reaction field that may be strong enough to alter the intermolecular structure (potential-energy surface) of the relatively floppy CT state of the complex. Specifically, the reaction field should favor a CT-state structure of a larger dipole moment by pulling $\text{D}^+–\text{A}^-$ farther apart to attain a lower free energy. In other words, the reaction field can “polarize” the CT complex by changing its structure. This tendency is counterbalanced by the attraction force between D^+ and A^- , resulting in a barrier to SSIP formation that must involve simultaneous dissociation and solvation of the ion pair. For typical covalently bonded rigid DA molecular systems, this interaction is probably too weak to produce noticeable structural change. The increasing ion-pair separation with the extent of solvation has been demonstrated theoretically and experimentally in microsolvation systems.^{139–141} For example, the ion-pair “bond” distances ($r_{\text{Na}-\text{Cl}}$) in $\text{NaCl}-(\text{H}_2\text{O})_n$ microsolvated clusters have been shown to increase monotonically from 2.397 to 3.167 Å for $n = 0$ to 10 by hybrid ab initio calculations.¹⁴⁰

In the simple dielectric continuum theory, the Onsager reaction field (E_R) is given by¹⁴²

$$E_R = \frac{1}{4\pi\epsilon_0 a^3} \frac{2(\epsilon - 1)}{2\epsilon + 1} \mu \quad (4)$$

where μ is the dipole moment of a point dipole in a spherical cavity of radius a , and ϵ is the dielectric constant of the solvent. A rough and conservative estimation using $\mu = 10$ D and $a = 0.5$ nm¹⁴³ for the BZ–TCNE CT state in CH_2Cl_2 ($\epsilon = 8.9$) gives a reaction field of $\sim 2 \times 10^9$ V/m. The force acting on each ion by the reaction field is significant with respect to the soft intermolecular force constant of $\sim 2 \times 10^{-8}$ N/nm between D^+ and A^- .¹⁴⁴ Therefore, the reaction field is strong enough to alter the geometry of the CT state, even at the dielectric continuum level of theory, and lead to a new equilibrium structure under its influence. Specific solute–solvent interactions at the molecular level may enhance the effect, as exemplified by the $\text{NaCl}-(\text{H}_2\text{O})_n$ systems mentioned above.¹⁴⁰

Such a reaction-field-induced structural change requires relaxations along both solvent and $\text{D}–\text{A}$ intermolecular coordinates and, thus, may take a much longer time than solvent reorientations. It can be regarded as a secondary solvation process because the solvent structure must also undergo minor adjustments to cope with the new solute structure. A schematic diagram illustrating this process is shown in Figure 13. The basic idea is, in fact, similar to that proposed by Arnold et al.,^{136,137} except that the $\text{D}^+–\text{A}^-$ separation is not large enough to allow solvent insertions in our case. One can envision that in solvents of even higher polarities, this process may further lead to formations of SSIP and ion dissociation in

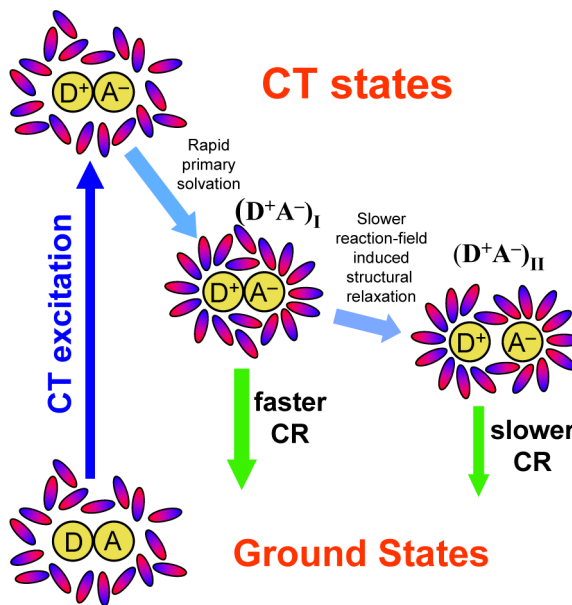


Figure 13. Schematic diagram illustrating the rapid primary solvation and the slower reaction-field-induced structural relaxation of an EDA complex upon CT excitation. The former involves mostly the solvent rearrangement; the latter involves relaxations along both solvent and D–A intermolecular coordinates. $(D^+-A^-)_I$ refers to the CT state after the primary solvation completes, typically in ~1 ps in simple dipolar aprotic solvents. $(D^+-A^-)_{II}$ refers to the fully relaxed CT-state structure under the influence of the reaction field. Not shown in the figure is the possible increase in the degree of charge separation along both relaxation steps.

longer time scales, provided that CR does not prevail. Note that the reaction field may also “polarize” the electronic wave function of the CT state and, thereby, increase the degree of charge separation. Such electronic response is expected to be much faster than nuclear relaxation and may follow closely with solvation.

Both the electronic coupling and emission transition moment depend on the overlap between HOMO and LUMO localized on D and A, respectively, and therefore, both CR and the emission rates are sensitive functions of relative orientations and distance between D^+ and A^- .^{47–49} It is usually assumed that the electronic coupling strength falls off exponentially with the D–A distance because of the exponential radial character of electronic wave functions.^{145,146} The emission transition moment probably follows the same dependence for the same reason. Indeed, it has been shown that, to a good approximation, the emission transition moment is proportional to the electronic coupling.^{147,148} The reaction-field-induced lengthening of the D^+-A^- separation is not large enough to accommodate solvent molecules and still allows substantial HOMO/LUMO overlaps; that is, unlike the SSIP, the fully solvated equilibrium CIP ($(D^+-A^-)_{II}$ in Figure 13) exhibits a reduced but nonnegligible emission rate. Thus, during the reaction-field-induced structural relaxation, the increase in D^+-A^- separation reduces HOMO/LUMO overlaps and leads to a decline in CR as well as emission rates.

A simplified kinetic model, shown in Figure 14A, is used to describe the CT-state relaxation dynamics in CH_2Cl_2 . In this model, $(D^+-A^-)_I$ refers to the CT state after the primary solvation is completed, typically in ~1 ps. At this point, the surrounding solvent molecules have rearranged to a free-energy

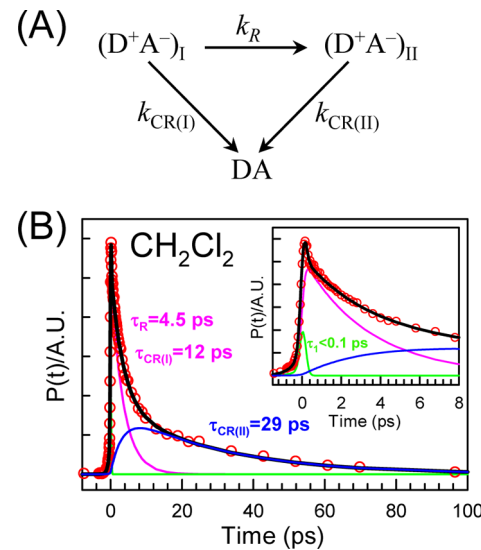


Figure 14. (A) CR kinetic model including the reaction-field-induced structural relaxation. (B) Fitting results using the kinetic model shown in (A) for $P(t)$ of BZ–TCNE in CH_2Cl_2 .

favored structure and a reaction field is formed. $(D^+-A^-)_{II}$ refers to the fully relaxed CT-state structure under the influence of the reaction field. Both $(D^+-A^-)_I$ and $(D^+-A^-)_{II}$ can undergo CR and radiative transitions back to the ground state (DA) but with different rates. $k_{\text{CR}(I)}$ and $k_{\text{CR}(II)}$ denote the CR rates of $(D^+-A^-)_I$ and $(D^+-A^-)_{II}$, respectively, whereas k_R is the relaxation rate from $(D^+-A^-)_I$ to $(D^+-A^-)_{II}$. With this simplified kinetic model, the fast fluorescence intensity decay of 3.2 ps observed in CH_2Cl_2 is simply $1/(k_{\text{CR}(I)} + k_R)$, and the slowest decay of 29 ps is $1/k_{\text{CR}(II)}$. Assuming that the radiative rate is proportional to the CR rate, the ratio of the emission rate constants of the two CT species is $k_{\text{rad}}(I)/k_{\text{rad}}(II) = k_{\text{CR}(I)}/k_{\text{CR}(II)}$. Under this constraint, the $P(t)$ function derived from the TRFL spectra in CH_2Cl_2 can be fit with this kinetic model convoluted with the IRF, which yielded $\tau_{\text{CR}(I)} = 12$ ps, $\tau_R = 4.6$ ps, and $\tau_{\text{CR}(II)} = 29$ ps.

This modeling suggests that when the primary solvation is completed in about 1 ps, the free energy of the CT state in CH_2Cl_2 decreases to such an extent that the CR rate is much faster (~12 ps). While undergoing rapid CR back to the neutral ground state, the system also rapidly relaxes under the influence of the reaction field to a new equilibrium structure, $(D^+-A^-)_{II}$, in which both the CR rate and emission intensity decrease by a factor of 2.4 because of a larger D–A separation. Thus, the biexponential decay of $P(t)$ in CH_2Cl_2 is, indeed, due to a nonequilibrium CR reaction, in which a major fraction of the CT-state population undergoes CR at a much faster rate prior to equilibrium.

In the case of CCl_4 and CHX, the reaction fields are expected to be much weaker. The dielectric continuum Onsager field of eq 4 predicts a reaction field in CCl_4 and CHX ~1.8 and 2.1 times weaker, respectively, than that in CH_2Cl_2 . On the other hand, because the dipole interaction energy with the reaction field is proportional to the field strength, the solvation contributions to the observed TDFSS in CCl_4 (~800 cm^{-1}) and CH_2Cl_2 (~4250 cm^{-1}) suggest that the reaction field in CCl_4 is ~2.5 times weaker than that in CH_2Cl_2 . The vanishing solvation contribution to TDFSS in CHX implies a much weaker reaction field in CHX. Therefore, the differences in CR and emission rates between $(D^+-A^-)_I$ and $(D^+-A^-)_{II}$ are

expected to be much smaller in the two nonpolar solvents. This is consistent with the observations that the $P(t)$ s obtained from TRFL spectra in CCl_4 and CHX data do not show noticeable biexponential decay behaviors. Instead, other effects due to vibrational/structural relaxation may become noticeable, as described below. Because the reaction-field-induced relaxation favors a complex structure with a larger dipole moment, additional spectral relaxation is expected and probably blended into the slowest component in TDFSS. This is consistent with the observations that the magnitude of the slowest TDFSS component is also solvent-dependent and is the greatest in CH_2Cl_2 .

Because the reaction-field-induced effect is counterbalanced by the attraction force between D^+ and A^- , the very weak reaction field in CHX implies a shorter D^+-A^- distance. This may explain the anomalous solvent effect of CR rates between CCl_4 and CHX; that is, the shorter D^+-A^- distance and, thus, a larger electronic coupling, in CHX not only compensates for the slightly larger driving force but also further makes the CR rate higher in CHX than in CCl_4 .

4.8. Vibrational Nonequilibrium Charge Recombination. As pointed out above, the initial temporal profile of $P(t)$ in the CCl_4 case remains nearly constant within a period of ~ 10 ps before embarking on the 150 ps exponential decay. Because the time scale (~ 10 ps) is similar to the slowest component in TDFSS relaxation, we propose that it is associated with the slow vibrational/structural relaxation. This type of nonexponential time profile can result from a small rise component, as modeled in the fit shown in Figure 9B, or an increasing CR rate with time. In either case, the results seem to suggest a small effect on CR dynamics due to vibrational relaxation.¹⁹ One possible interpretation is that it is due to an increasing CR rate following vibrational relaxation and is an indication of variations in CR rates with excitations in certain vibrational modes. For example, slow relaxation along some low-frequency inactive modes may lead to the observed behavior, that is, an increasing CR rate with time.

Another possible mechanism is related to the D–A structural dependence of the electronic coupling.^{47–49} As shown in Figure 12, our calculations predicted that the equilibrium structure of the BZ–TCNE CT1 state is quite different from that of the ground state. Specifically, in the CT1 state, the BZ and TCNE moieties are laterally shifted and the interplanar distance becomes shorter. In solutions, the D–A intermolecular potential is perturbed by solvent interactions and the D–A separation shortening may be counterbalanced by the reaction field. Vertical CT excitation creates an initial BZ–TCNE structure distribution centered at the symmetric configuration, which then slowly relaxes to one that centers at the laterally distorted geometry. During such relaxation, the average electronic coupling and emission transition moment also evolve. Specifically, the C_{2v} structure of the CT1 state has zero electronic coupling and emission transition moment by symmetry, although the large-amplitude intermolecular motion should allow both CR and emission to gain appreciable probabilities. On the other hand, as suggested by the calculated oscillator strengths (Table 4), when the CT1 state is stabilized at the distorted equilibrium structure, the average emission transition moment and electronic coupling are enhanced as a result of the lowered symmetry. Increases in both CR and emission rates during the relaxation from the FC to equilibrium structures can give rise to the observed nonexponential time profile in CCl_4 (Figure 9B).

It is likely that both mechanisms are operative simultaneously in the present case. In either case, a small fraction of the CT-state population undergoes CR prior to vibrational equilibrium in CCl_4 and manifests the effect of intramolecular vibrations on CR dynamics. In the case of CH_2Cl_2 , the fraction undergoing vibrational nonequilibrium CR is much higher because of the much faster CR rates. Unfortunately, the corresponding nonexponential feature is probably overwhelmed by the stronger effect of the reaction-field-induced structural relaxation discussed above. Only when the reaction field is minimal can the subtle effects on CR dynamics due to vibrational/structural relaxation be revealed.

5. CONCLUSIONS

We have presented in this work a thorough study of the CT-state dynamics of the BZ–TCNE complex in three solvents of different polarities with ultrafast broadband TRFL spectroscopy implemented by optical Kerr gating. Temporal and spectral evolutions of the fluorescence were observed and analyzed to elucidate various relaxation processes following initial CT excitation. The general picture emerging from these results is that the initial CT-state dynamics is dominated by rapid relaxations along both solvent and vibrational coordinates, followed by slower charge recombination reactions. By comparing the results in solvents of different polarities, we partially separated solvation and vibrational relaxation dynamics and explored the solvent-dependent CR dynamics. The biphasic and slow time scales of the vibrational contributions identified in TDFSS suggested the presence of nonstatistical and hindered IVR that can be attributed to the unique structural properties of EDA complexes. The slowest spectral relaxations of 10–15 ps identified in TDFSS are assigned to relaxation of D–A intermolecular vibrations, which is equivalent to a structural relaxation from the initial FC configuration to the equilibrium CT-state structure. The time scales of vibrational relaxation indicate that a fraction of the CT-state population undergoes CR reactions before complete vibrational/structural equilibrium is achieved. In CCl_4 , an initial nonexponential behavior was observed and attributed to vibrational nonequilibrium CR. In polar CH_2Cl_2 solvent, the strong polar solvation greatly accelerates the CR reactions. A reaction-field-induced structural relaxation leading to an equilibrium configuration of longer D^+-A^- separations is proposed to account for the pronounced biexponential decay observed only in CH_2Cl_2 . Equilibrium CR time constants for BZ–TCNE CT state in CH_2Cl_2 , CCl_4 , and CHX are 29, 150, and 68 ps, respectively, which are generally in line with the expectation for the Marcus inverted region. The unexpected reversed $-\Delta G^\circ$ dependence between the equilibrium CR rates observed in CCl_4 and CHX suggest that the CT-state structures of EDA complexes are strongly solvent-dependent and must be taken into account when comparing ET rates in different solvents.

■ ASSOCIATED CONTENT

S Supporting Information

Procedures for correcting spectral sensitivity and temporal dispersion of TRFL spectra. Justifications of the assignments of spectra to the 1:1 BZ–TCNE complex. Lists of calculated vibrational modes with frequencies below 200 cm^{-1} for the BZ–TCNE ground and excited states. Vibrational displacement vectors of the three lowest frequency modes. HOMO, HOMO-

1, and LUMO at the ground-state structure. This information is available free of charge via the Internet at <http://pubs.acs.org>

AUTHOR INFORMATION

Corresponding Author

*E-mail: pycheng@mx.nthu.edu.tw.

Notes

The authors declare no competing financial interest.

ACKNOWLEDGMENTS

This work was supported by the National Science Council of Taiwan, Republic of China.

REFERENCES

- (1) Kuznetsov, A. M. *Charge Transfer in Physics, Chemistry, and Biology*; Gordon & Breach: Amsterdam, 1995.
- (2) Hagfeldt, A.; Boschloo, G.; Sun, L.; Kloo, L.; Pettersson, H. Dye-Sensitized Solar Cells. *Chem. Rev.* **2010**, *110*, 6595–6663.
- (3) Jennings, J. R.; Liu, Y.; Wang, Q.; Zakeeruddin, S. M.; Gratzel, M. The Influence of Dye Structure on Charge Recombination in Dye-Sensitized Solar Cells. *Phys. Chem. Chem. Phys.* **2011**, *13*, 6637–6648.
- (4) Maggio, E.; Martsinovich, N.; Troisi, A. Evaluating Charge Recombination Rate in Dye-Sensitized Solar Cells from Electronic Structure Calculations. *J. Phys. Chem. C* **2012**, *116*, 7638–7649.
- (5) Mulliken, R. S.; Person, W. B. Donor–Acceptor Complexes. *Annu. Rev. Phys. Chem.* **1962**, *13*, 107–126.
- (6) Foster, R. *Organic Charge-Transfer Complexes*; Academic Press: New York, 1969.
- (7) Mataga, N.; Kubota, T. *Molecular Interactions and Electronic Spectra*; Marcel Dekker, Inc.: New York, 1970; Chapter 6.
- (8) Brouwer, F. Structural Aspects of Exciplex Formation. In *Conformational Analysis of Molecules in Excited States*; Waluk, J., Ed.; Wiley-VCH, Inc.: New York, 2000; pp 177–235.
- (9) Gould, I. R.; Farid, S. Dynamics of Bimolecular Photoinduced Electron-Transfer Reactions. *Acc. Chem. Res.* **1996**, *29*, 522–528.
- (10) Mataga, N.; Chosrowjan, H.; Taniguchi, S. Ultrafast Charge Transfer in Excited Electronic States and Investigations into Fundamental Problems of Exciplex Chemistry: Our Early Studies and Recent Developments. *J. Photochem. Photobiol. C* **2005**, *6*, 37–79.
- (11) Cheng, P. Y.; Zhong, D.; Zewail, A. H. Femtosecond Real-Time Probing of Reactions. 21. Direct Observation of Transition-State Dynamics and Structure in Charge-Transfer Reactions. *J. Chem. Phys.* **1996**, *105*, 6216–6248.
- (12) Zhong, D. P.; Bernhardt, T. M.; Zewail, A. H. Femtosecond Real-Time Probing of Reactions. 24. Time, Velocity, and Orientation Mapping of the Dynamics of Dative Bonding in Bimolecular Electron Transfer Reactions. *J. Phys. Chem. A* **1999**, *103*, 10093–10117.
- (13) Fiebig, T.; Wan, C. Z.; Kelley, S. O.; Barton, J. K.; Zewail, A. H. Femtosecond Dynamics of the DNA Intercalator Ethidium and Electron Transfer with Mononucleotides in Water. *Proc. Natl. Acad. Sci. U.S.A.* **1999**, *96*, 1187–1192.
- (14) Maroncelli, M.; Macinnis, J.; Fleming, G. R. Polar-Solvent Dynamics and Electron-Transfer Reactions. *Science* **1989**, *243*, 1674–1681.
- (15) Sumi, H.; Marcus, R. A. Dynamic Effects in Electron-Transfer Reactions. *J. Chem. Phys.* **1986**, *84*, 4894–4914.
- (16) Jortner, J.; Bixon, M. Intramolecular Vibrational Excitations Accompanying Solvent-Controlled Electron-Transfer Reactions. *J. Chem. Phys.* **1988**, *88*, 167–170.
- (17) Walker, G. C.; Akesson, E.; Johnson, A. E.; Levinger, N. E.; Barbara, P. F. Interplay of Solvent Motion and Vibrational-Excitation in Electron-Transfer Kinetics - Experiment and Theory. *J. Phys. Chem.* **1992**, *96*, 3728–3736.
- (18) Gayathri, N.; Bagchi, B. Quantum and Non-Markovian Effects in the Electron Transfer Reaction Dynamics in the Marcus Inverted Region. *J. Phys. Chem.* **1996**, *100*, 3056–3062.
- (19) Denny, R. A.; Bagchi, B.; Barbara, P. F. Effects of Vibrational Energy Relaxation and Reverse Reaction on Electron Transfer Kinetics and Fluorescence Line Shapes in Solution. *J. Chem. Phys.* **2001**, *115*, 6058–6071.
- (20) Bagchi, B.; Gayathri, N. Interplay Between Ultrafast Polar Solvation and Vibrational Dynamics in Electron Transfer Reactions: Role of High-Frequency Vibrational Modes. *Adv. Chem. Phys.* **1999**, *107*, 1–80.
- (21) Yudanov, V. V.; Mikhailova, V. A.; Ivanov, A. I. Reorganization of Intramolecular High Frequency Vibrational Modes and Dynamic Solvent Effect in Electron Transfer Reactions. *J. Phys. Chem. A* **2012**, *116*, 4010–4019.
- (22) Ionkin, V. N.; Ivanov, A. I. Independence of the Rate of the Hot Charge Recombination in Excited Donor–Acceptor Complexes from the Spectral Density of High-Frequency Vibrations. *Chem. Phys.* **2009**, *360*, 137–140.
- (23) Feskov, S. V.; Ionkin, V. N.; Ivanov, A. I. Effect of High-Frequency Modes and Hot Transitions on Free Energy Gap Dependence of Charge Recombination Rate. *J. Phys. Chem. A* **2006**, *110*, 11919–11925.
- (24) Barbara, P. F.; Walker, G. C.; Smith, T. P. Vibrational-Modes and the Dynamic Solvent Effect in Electron and Proton-Transfer. *Science* **1992**, *256*, 975–981.
- (25) Nagasawa, Y.; Yartsev, A. P.; Tominaga, K.; Bisht, P. B.; Johnson, A. E.; Yoshihara, K. Dynamical Aspects of Ultrafast Intermolecular Electron-Transfer Faster Than Solvation Process — Substituent Effects and Energy-Gap Dependence. *J. Phys. Chem.* **1995**, *99*, 653–662.
- (26) Akesson, E.; Walker, G. C.; Barbara, P. F. Dynamic Solvent Effects on Electron-Transfer Rates in the Inverted Regime — Ultrafast Studies on the Betaines. *J. Chem. Phys.* **1991**, *95*, 4188–4194.
- (27) Wan, C. Z.; Xia, T. B.; Becker, H. C.; Zewail, A. H. Ultrafast Unequilibrated Charge Transfer: A New Channel in the Quenching of Fluorescent Biological Probes. *Chem. Phys. Lett.* **2005**, *412*, 158–163.
- (28) Kulinowski, K.; Gould, I. R.; Ferris, N. S.; Myers, A. B. Spectroscopic, Kinetic, and Thermodynamic Deuterium Isotope Effects in the Hexamethylbenzene/Tetracyanoethylene Charge-Transfer Complex. *J. Phys. Chem.* **1995**, *99*, 17715–17723.
- (29) Myers, A. B. Resonance Raman Intensities and Charge-Transfer Reorganization Energies. *Chem. Rev.* **1996**, *96*, 911–926.
- (30) Hayashi, M.; Yang, T. S.; Yu, J.; Mebel, A.; Lin, S. H. On the Theoretical Investigation on Spectroscopy of the Electron Donor–Acceptor Complex TCNE-HMB. *J. Phys. Chem. A* **1997**, *101*, 4156–4162.
- (31) Cox, M. J.; Crim, F. F. Vibrational Energy Flow Rates for Cis- and Trans-Stilbene Isomers in Solution. *J. Phys. Chem. A* **2005**, *109*, 11673–11678.
- (32) Charvat, A.; Assmann, J.; Abel, B.; Schwarzer, D.; Henning, K.; Luther, K.; Troe, J. Direct Observation of Intramolecular Vibrational Energy Redistribution of Selectively Excited CH_2I_2 and $\text{C}_3\text{H}_5\text{I}$ Molecules in Solution. *Phys. Chem. Chem. Phys.* **2001**, *3*, 2230–2240.
- (33) Assmann, J.; Kling, M.; Abel, B. Watching Photoinduced Chemistry and Molecular Energy Flow in Solution in Real Time. *Angew. Chem., Int. Ed.* **2003**, *42*, 2226–2246.
- (34) Weigel, A.; Ernsting, N. P. Excited Stilbene: Intramolecular Vibrational Redistribution and Solvation Studied by Femtosecond Stimulated Raman Spectroscopy. *J. Phys. Chem. B* **2010**, *114*, 7879–7893.
- (35) Assmann, J.; von Benten, R.; Charvat, A.; Abel, B. Intra- and Intermolecular Vibrational Energy Relaxation of C–H Overtone Excited Benzonitrile, para-Difluorobenzene, and Pyrazine in Solution. *J. Phys. Chem. A* **2003**, *107*, 5291–5297.
- (36) Assmann, J.; von Benten, R.; Charvat, A.; Abel, B. Vibrational Energy Relaxation of Selectively Excited Aromatic Molecules in Solution: The Effect of a Methyl Rotor and its Chemical Substitution. *J. Phys. Chem. A* **2003**, *107*, 1904–1913.
- (37) Iwaki, L. K.; Deak, J. C.; Rhea, S. T.; Dlott, D. D. Vibrational Energy Redistribution in Liquid Benzene. *Chem. Phys. Lett.* **1999**, *303*, 176–182.

- (38) Seong, N. H.; Fang, Y.; Dlott, D. D. Vibrational Energy Dynamics of Normal and Deuterated Liquid Benzene. *J. Phys. Chem. A* **2009**, *113*, 1445–1452.
- (39) Pein, B. C.; Seong, N. H.; Dlott, D. D. Vibrational Energy Relaxation of Liquid Aryl-Halides X–C₆H₅ (X = F, Cl, Br, I). *J. Phys. Chem. A* **2010**, *114*, 10500–10507.
- (40) Iwata, K.; Hamaguchi, H. Microscopic Mechanism of Solute-Solvent Energy Dissipation Probed by Picosecond Time-Resolved Raman Spectroscopy. *J. Phys. Chem. A* **1997**, *101*, 632–637.
- (41) Sarkar, N.; Takeuchi, S.; Tahara, T. Vibronic Relaxation of Polyatomic Molecule in Nonpolar Solvent: Femtosecond Anisotropy Intensity Measurements of the S_n and S₁ Fluorescence of Tetracene. *J. Phys. Chem. A* **1999**, *103*, 4808–4814.
- (42) Nicolet, O.; Banerji, N.; Pages, S.; Vauthey, E. Effect of the Excitation Wavelength on the Ultrafast Charge Recombination Dynamics of Donor–Acceptor Complexes in Polar Solvents. *J. Phys. Chem. A* **2005**, *109*, 8236–8245.
- (43) Feskov, S. V.; Ionkin, V. N.; Ivanov, A. I.; Hagemann, H.; Vauthey, E. Solvent and Spectral Effects in the Ultrafast Charge Recombination Dynamics of Excited Donor–Acceptor Complexes. *J. Phys. Chem. A* **2008**, *112*, 594–601.
- (44) Kao, Y. T.; Guo, X. M.; Yang, Y.; Liu, Z. Y.; Hassanali, A.; Song, Q. H.; Wang, L. J.; Zhong, D. P. Ultrafast Dynamics of Non-equilibrium Electron Transfer in Photoinduced Redox Cycle: Solvent Mediation and Conformation Flexibility. *J. Phys. Chem. B* **2012**, *116*, 9130–9140.
- (45) Fujisawa, T.; Creelman, M.; Mathies, R. A. Structural Dynamics of a Noncovalent Charge Transfer Complex from Femtosecond Stimulated Raman Spectroscopy. *J. Phys. Chem. B* **2012**, *116*, 10453–10460.
- (46) Bauer, C.; Teuscher, J.; Pelet, S.; Wenger, B.; Bonhote, P.; Nazeeruddin, M. K.; Zakeeruddin, S. M.; Comte, P.; Gratzel, M.; Moser, J. E. Ultrafast Charge Transfer Through *p*-Oligo(phenylene) Bridges: Effect of Nonequilibrium Vibrations. *Curr. Sci.* **2010**, *99*, 343–352.
- (47) Ohta, K.; Closs, G. L.; Morokuma, K.; Green, N. J. Stereoelectronic Effects in Intramolecular Long-Distance Electron Transfer in Radical Anions as Predicted by Ab-Initio MO Calculations. *J. Am. Chem. Soc.* **1986**, *108*, 1319–1320.
- (48) Hsu, C. P. The Electronic Couplings in Electron Transfer and Excitation Energy Transfer. *Acc. Chem. Res.* **2009**, *42*, 509–518.
- (49) Kistler, K. A.; Spano, F. C.; Matsika, S. A Benchmark of Excitonic Couplings Derived from Atomic Transition Charges. *J. Phys. Chem. B* **2013**, *117*, 2032–2044.
- (50) Merrifield, R. E.; Phillips, W. D. Cyanocarbon Chemistry. II Spectroscopic Studies of the Molecular Complexes of TCNE. *J. Am. Chem. Soc.* **1958**, *80*, 2778–2782.
- (51) Voigt, E. M. Multiple Charge-Transfer Bands in Complexes Involving Aromatic Donors. *J. Am. Chem. Soc.* **1964**, *86*, 3611–3617.
- (52) Foster, R. Electron Donor–Acceptor Complexes. *J. Phys. Chem.* **1980**, *84*, 2135–2141.
- (53) Frey, J. E.; Andrews, A. M.; Ankoviak, D. G.; Beaman, D. N.; Dupont, L. E.; Elsner, T. E.; Lang, S. R.; Zwart, M. A. O.; Seagle, R. E.; Torreano, L. A. Charge-Transfer Complexes of Tetracyanoethylene with Cycloalkanes, Alkenes, and Alkynes and Some of Their Aryl Derivatives. *J. Org. Chem.* **1990**, *55*, 606–624.
- (54) Jarzeba, W.; Murata, S.; Tachiya, M. Ultrafast Dynamics of the Excited Tetracyanoethylene–Toluene Electron Donor–Acceptor Complex. *Chem. Phys. Lett.* **1999**, *301*, 347–355.
- (55) Britt, B. M.; McHale, J. L.; Friedrich, D. M. Application of Time-Dependent Raman Theory to Raman Excitation Profiles of Hexamethylbenzene–Tetracyanoethylene Electron-Donor Acceptor Complex. *J. Phys. Chem.* **1995**, *99*, 6347–6355.
- (56) Kimura, Y.; Takebayashi, Y.; Hirota, N. Electron-Transfer Rate in the Hexamethylbenzene–Tetracyanoethylene Charge-Transfer Complex in Carbon Dioxide. *Chem. Phys. Lett.* **1996**, *257*, 429–433.
- (57) Wynne, K.; Galli, C.; Hochstrasser, R. M. Ultrafast Charge-Transfer in an Electron Donor–Acceptor Complex. *J. Chem. Phys.* **1994**, *100*, 4797–4810.
- (58) Rubtsov, I. V.; Yoshihara, K. Oscillatory Fluorescence Decay of an Electron Donor–Acceptor Complex. *J. Phys. Chem. A* **1997**, *101*, 6138–6140.
- (59) Rubtsov, I. V.; Yoshihara, K. Vibrational Coherence in Electron Donor–Acceptor Complexes. *J. Phys. Chem. A* **1999**, *103*, 10202–10212.
- (60) Zhou, J. W.; Findley, B. R.; Teslja, A.; Braun, C. L.; Sutin, N. Ion Pairs From Photoexcited, “Random” Electron Donors and Acceptors: Alkylbenzenes and Tetracyanoethylene. *J. Phys. Chem. A* **2000**, *104*, 11512–11521.
- (61) Yamamoto, K.; Kabir, M. H.; Hayashi, M.; Tominaga, K. Low-Frequency Spectra of the Hexamethylbenzene/Tetracyanoethylene Electron Donor–Acceptor Complexes in Solution Studied by Terahertz Time-Domain Spectroscopy. *Phys. Chem. Chem. Phys.* **2005**, *7*, 1945–1952.
- (62) Markel, F.; Ferris, N. S.; Gould, I. R.; Myers, A. B. Mode-Specific Vibrational Reorganization Energies Accompanying Photo-induced Electron-Transfer in the Hexamethylbenzene Tetracyanoethylene Charge-Transfer Complex. *J. Am. Chem. Soc.* **1992**, *114*, 6208–6219.
- (63) Kimura, Y.; Takebayashi, Y.; Hirota, N. Effect of the Solvent Density and Species on the Back-Electron Transfer Rate in the Hexamethylbenzene/Tetracyanoethylene Charge-Transfer Complex. *J. Chem. Phys.* **1998**, *108*, 1485–1498.
- (64) Hayashi, M.; Yang, T. S.; Yu, J.; Mebel, A.; Chang, R.; Lin, S. H.; Rubtsov, I. V.; Yoshihara, K. Vibronic and Vibrational Coherence and Relaxation Dynamics in the TCNE–HMB Complex. *J. Phys. Chem. A* **1998**, *102*, 4256–4265.
- (65) Kysel, O.; Budzak, S.; Mach, P.; Medved, M. MP2 and DFT Study of IR Spectra of TCNE–Methylsubstituted Benzene Complexes: Is Charge Transfer Important? *Int. J. Quantum Chem.* **2010**, *110*, 1712–1728.
- (66) Kysel, O.; Budzak, S.; Medved, M.; Mach, P. MP2, DFT-D, and PCM Study of the HMB–TCNE Complex: Thermodynamics, Electric Properties, and Solvent Effects. *Int. J. Quantum Chem.* **2008**, *108*, 1533–1545.
- (67) Kuchenbecker, D.; Jansen, G. Intermolecular Interactions in Weak Donor–Acceptor Complexes from Symmetry-Adapted Perturbation and Coupled-Cluster Theory: Tetracyanoethylene–Benzene and Tetracyanoethylene–*p*-Xylene. *ChemPhysChem* **2012**, *13*, 2769–2776.
- (68) Mach, P.; Budzak, S.; Medved, M.; Kysel, O. Theoretical Analysis of Charge-Transfer Electronic Spectra of Methylated Benzenes–TCNE Complexes Including Solvent Effects: Approaching Experiment. *Theor. Chem. Acc.* **2012**, *131*, 1268–1281.
- (69) Kroll, M. Molecular Complexes and Their Spectra 0.20. Gas-Phase Electron Donor–Acceptor Complexes. *J. Am. Chem. Soc.* **1968**, *90*, 1097–1105.
- (70) Herndon, W. C.; Feuer, J.; Mitchell, R. E. Calorimetric Studies of π -Molecular Complexes — Tetracyanoethylene and Aromatic Donors. *J. Chem. Soc. D: Chem. Commun.* **1971**, 435–435.
- (71) Hanazaki, I. Vapor-Phase Electron Donor–Acceptor Complexes of Tetracyanoethylene and of Sulfur Dioxide. *J. Phys. Chem.* **1972**, *76*, 1982–1989.
- (72) Hubig, S. M.; Bockman, T. M.; Kochi, J. K. Optimized Electron Transfer in Charge-Transfer Ion Pairs. Pronounced Inner-Sphere Behavior of Olefin Donors. *J. Am. Chem. Soc.* **1996**, *118*, 3842–3851.
- (73) Schmidt, B.; Laimgruber, S.; Zinth, W.; Gilch, P. A Broadband Kerr Shutter for Femtosecond Fluorescence Spectroscopy. *Appl. Phys. B* **2003**, *76*, 809–814.
- (74) Arzhantsev, S.; Maroncelli, M. Design and Characterization of a Femtosecond Fluorescence Spectrometer Based on Optical Kerr Gating. *Appl. Spectrosc.* **2005**, *59*, 206–220.
- (75) Nakamura, R.; Kanematsu, Y. Femtosecond Spectral Snapshots Based on Electronic Optical Kerr Effect. *Rev. Sci. Instrum.* **2004**, *75*, 636–644.
- (76) Maroncelli, M.; Fleming, G. R. Picosecond Solvation Dynamics of Coumarin-153 — The Importance of Molecular Aspects of Solvation. *J. Chem. Phys.* **1987**, *86*, 6221–6239.

- (77) Sharp spectral features in the $\lambda < 440$ nm region due to spontaneous Raman scattering of the solvent in the early time raw TRFL spectra have been subtracted. Small dips at about 620 nm due to the inverse Raman scattering arising from the interaction between the fluorescence and the gate pulse in the Kerr medium have also been removed.
- (78) The most intense Raman bands near 430 nm are more than 1000 times stronger than BZ–TCNE complex fluorescence in CHX! It arises from the combined signals of several closely spaced Raman lines of the CHX solvent near ~ 2900 cm⁻¹. Weaker Raman combination and overtone bands of CHX were also observed at longer wavelengths. These interferences made the TRFL spectra before ~ 1 ps difficult to analyze. In the case of CCl₄ as the solvent, the complex concentration is also very low, but because vibrational frequencies of CCl₄ are much lower, only the weak Raman combination and overtone bands overlap with BZ–TCNE fluorescence spectra and can be easily removed.
- (79) Horng, M. L.; Gardecki, J. A.; Papazyan, A.; Maroncelli, M. Subpicosecond Measurements of Polar Solvation Dynamics — Coumarin 153 Revisited. *J. Phys. Chem.* **1995**, *99*, 17311–17337.
- (80) Gustavsson, T.; Cassara, L.; Gulbinas, V.; Gurzadyan, G.; Mialocq, J. C.; Pommeret, S.; Sorgius, M.; van der Meulen, P. Femtosecond Spectroscopic Study of Relaxation Processes of Three Amino-Substituted Coumarin Dyes in Methanol and Dimethyl Sulfoxide. *J. Phys. Chem. A* **1998**, *102*, 4229–4245.
- (81) Gustavsson, T.; Baldacchino, G.; Mialocq, J. C.; Pommeret, S. A Femtosecond Fluorescence Up-Conversion Study of the Dynamic Stokes Shift of the DCM Dye Molecule in Polar and Nonpolar Solvents. *Chem. Phys. Lett.* **1995**, *236*, 587–594.
- (82) Pigliucci, A.; Duvanel, G.; Daku, L. M. L.; Vauthay, E. Investigation of the Influence of Solute–Solvent Interactions on the Vibrational Energy Relaxation Dynamics of Large Molecules in Liquids. *J. Phys. Chem. A* **2007**, *111*, 6135–6145.
- (83) Jin, H.; Liang, M.; Arzhantsev, S.; Li, X.; Maroncelli, M. Photophysical Characterization of Benzylidene Malononitriles as Probes of Solvent Friction. *J. Phys. Chem. B* **2010**, *114*, 7565–7578.
- (84) Maroncelli, M.; Fee, R. S.; Chapman, C. F.; Fleming, G. R. Dynamic Stokes Shift in Coumarin — Is It Only Relaxation — Comment. *J. Phys. Chem.* **1991**, *95*, 1012–1014.
- (85) Kanya, R.; Ohshima, Y. Determination of Dipole Moment Change on the Electronic Excitation of Isolated Coumarin 153 by Pendular-State Spectroscopy. *Chem. Phys. Lett.* **2003**, *370*, 211–217.
- (86) Kumar, P. V.; Maroncelli, M. Polar Solvation Dynamics of Polyatomic Solutes — Simulation Studies in Acetonitrile and Methanol. *J. Chem. Phys.* **1995**, *103*, 3038–3060.
- (87) Stratt, R. M.; Maroncelli, M. Nonreactive Dynamics in Solution: The Emerging Molecular View of Solvation Dynamics and Vibrational Relaxation. *J. Phys. Chem.* **1996**, *100*, 12981–12996.
- (88) Eom, I.; Joo, T. Polar Solvation Dynamics of Coumarin 153 by Ultrafast Time-Resolved Fluorescence. *J. Chem. Phys.* **2009**, *131*, 244507–244507.
- (89) Reynolds, L.; Gardecki, J. A.; Frankland, S. J. V.; Horng, M. L.; Maroncelli, M. Dipole Solvation in Nondipolar Solvents: Experimental Studies of Reorganization Energies and Solvation Dynamics. *J. Phys. Chem.* **1996**, *100*, 10337–10354.
- (90) Frisch, M. J.; Trucks, G. W.; Schlegel, H. B.; Scuseria, G. E.; Robb, M. A.; Cheeseman, J. R.; Scalmani, G.; Barone, V.; Mennucci, B.; Petersson, G. A., et al. Gaussian 09, Revision A.02; Gaussian, Inc.: Wallingford, CT, USA, 2009.
- (91) Zhao, Y.; Truhlar, D. G. Density Functional for Spectroscopy: No Long-Range Self-Interaction Error, Good Performance for Rydberg and Charge-Transfer States, and Better Performance on Average than B3LYP for Ground States. *J. Phys. Chem. A* **2006**, *110*, 13126–13130.
- (92) Emery, L. C.; Sheldon, J. M.; Edwards, W. D.; McHale, J. L. Intermolecular Ground and Excited-State Potential-Energy Surfaces and Charge-Transfer Spectrum of Benzene–TCNE Electron-Donor Acceptor Complex. *Spectrochim. Acta A* **1992**, *48*, 715–724.
- (93) Glauser, W. A.; Raber, D. J.; Stevens, B. Electron-Donor Acceptor Orbital Correlations. 8. Selection Rules for Vibrational Enhancement of Intermolecular Electron Transfer. *J. Phys. Chem.* **1991**, *95*, 1976–1979.
- (94) Fee, R. S.; Maroncelli, M. Estimating the Time-Zero Spectrum in Time-Resolved Emission Measurements of Solvation Dynamics. *Chem. Phys.* **1994**, *183*, 235–247.
- (95) Ajdarzadeh Oskouei, A.; Braem, O.; Cannizzo, A.; van Mourik, F.; Tortschanoff, A.; Chergui, M. Ultrafast UV Photon Echo Peak Shift and Fluorescence Up Conversion Studies of Non-Polar Solvation Dynamics. *Chem. Phys.* **2008**, *350*, 104–110.
- (96) Reichardt, C. Solvatochromic Dyes as Solvent Polarity Indicators. *Chem. Rev.* **1994**, *94*, 2319–2358.
- (97) Laurence, C.; Nicolet, P.; Dalati, M. T.; Abboud, J. L. M.; Notario, R. The Empirical Treatment of Solvent Solute Interactions — 15 Years of Pi. *J. Phys. Chem.* **1994**, *98*, 5807–5816.
- (98) Kamlet, M. J.; Abboud, J. L. M.; Abraham, M. H.; Taft, R. W. Linear Solvation Energy Relationships. 23. A Comprehensive Collection of the Solvatochromic Parameters, Pi-Star, Alpha and Beta, and Some Methods for Simplifying the Generalized Solvatochromic Equation. *J. Org. Chem.* **1983**, *48*, 2877–2887.
- (99) Kovalenko, S. A.; Ruthmann, J.; Ernsting, N. P. Ultrafast Stokes Shift and Excited-State Transient Absorption of Coumarin 153 in Solution. *Chem. Phys. Lett.* **1997**, *271*, 40–50.
- (100) Loring, R. F.; Yan, Y. J.; Mukamel, S. Time-Resolved Fluorescence and Hole-Burning Line Shapes of Solvated Molecules — Longitudinal Dielectric-Relaxation and Vibrational Dynamics. *J. Chem. Phys.* **1987**, *87*, 5840–5857.
- (101) Yu, A. C.; Tolbert, C. A.; Farrow, D. A.; Jonas, D. M. Solvatochromism and Solvation Dynamics of Structurally Related Cyanine Dyes. *J. Phys. Chem. A* **2002**, *106*, 9407–9419.
- (102) Kovalenko, S. A.; Ernsting, N. P.; Ruthmann, J. Femtosecond Stokes Shift in Styryl Dyes: Solvation or Intramolecular Relaxation? *J. Chem. Phys.* **1997**, *106*, 3504–3511.
- (103) Karunakaran, V.; Lustres, J. L. F.; Zhao, L. J.; Ernsting, N. P.; Seitz, O. Large Dynamic Stokes Shift of DNA Intercalation Dye Thiazole Orange Has Contribution From a High-Frequency Mode. *J. Am. Chem. Soc.* **2006**, *128*, 2954–2962.
- (104) Agmon, N. Dynamic Stokes Shift in Coumarin: Is It Only Relaxation? *J. Phys. Chem.* **1990**, *94*, 2959–2963.
- (105) The mean emission frequency at time zero reported in this work is that obtained with the deconvolution procedures described in section 3.4.
- (106) Nakamura, R.; Wang, P.; Fujii, R.; Koyama, Y.; Hashimoto, H.; Kanematsu, Y. Vibrational Relaxation Pathways in the Electronic Excited State of Carotenoid. *J. Lumin.* **2006**, *119*, 442–447.
- (107) Nakamura, R.; Hamada, N.; Ichida, H.; Tokunaga, F.; Kanematsu, Y. Transient Vibronic Structure in Ultrafast Fluorescence Spectra of Photoactive Yellow Protein. *Photochem. Photobiol.* **2008**, *84*, 937–940.
- (108) Coveleskie, R. A.; Dolson, D. A.; Parmenter, C. S. Chemical Timing. 2. The Picosecond Dynamics of Intramolecular Vibrational Redistribution in S₁ Para-Difluorobenzene. *J. Phys. Chem.* **1985**, *89*, 655–665.
- (109) Holtzclaw, K. W.; Parmenter, C. S. A Time-Resolved Fluorescence Search for Intramolecular Vibrational Redistribution in S₁ para-Difluorobenzene Vapor. *J. Phys. Chem.* **1984**, *88*, 3182–3185.
- (110) Holtzclaw, K. W.; Parmenter, C. S. Chemical Timing. 3. The Picosecond Dynamics of Intramolecular Vibrational Redistribution from 11 Levels in S₁-para-Difluorobenzene Vapor. *J. Chem. Phys.* **1986**, *84*, 1099–1118.
- (111) Mokhtari, A.; Chesnay, J.; Laubereau, A. Femtosecond Time-Resolved and Frequency-Resolved Fluorescence Spectroscopy of a Dye Molecule. *Chem. Phys. Lett.* **1989**, *155*, 593–598.
- (112) Sajadi, M.; Dobryakov, A. L.; Garbin, E.; Ernsting, N. P.; Kovalenko, S. A. Time-Resolved Fluorescence Spectra of cis-Stilbene in Hexane and Acetonitrile. *Chem. Phys. Lett.* **2010**, *489*, 44–47.
- (113) 0–0 Transition frequency for C153 in CH₂Cl₂ was estimated to be at ~ 22200 cm⁻¹ by locating the crossing point of reduced

- absorption spectrum and TRFL spectrum near time zero where polar solvation is minimal.
- (114) Shaffer, C. J.; Revesz, A.; Schroder, D.; Severa, L.; Teply, F.; Zins, E. L.; Jasikova, L.; Roithova, J. Can Hindered Intramolecular Vibrational Energy Redistribution Lead to Non-Ergodic Behavior of Medium-Sized Ion Pairs? *Angew. Chem., Int. Ed.* **2012**, *51*, 10050–10053.
- (115) Kim, J. E.; Tauber, M. J.; Mathies, R. A. Analysis of the Mode-Specific Excited-State Energy Distribution and Wavelength-Dependent Photoreaction Quantum Yield in Rhodopsin. *Biophys. J.* **2003**, *84*, 2492–2501.
- (116) Cheatum, C. M.; Heckscher, M. M.; Bingemann, D.; Crim, F. F. CH_2I_2 Fundamental Vibrational Relaxation in Solution Studied by Transient Electronic Absorption Spectroscopy. *J. Chem. Phys.* **2001**, *115*, 7086–7093.
- (117) von Benten, R.; Link, O.; Abel, B.; Schwarzer, D. The Impact of a Solvent and a Methyl Rotor on Timescales of Intramolecular Vibrational Energy Redistribution in Aromatic Molecules. *J. Phys. Chem. A* **2004**, *108*, 363–367.
- (118) von Benten, R. S.; Abel, B. On the Nature of Intramolecular Vibrational Energy Transfer in Dense Molecular Environments. *Chem. Phys.* **2010**, *378*, 19–26.
- (119) Gruebele, M.; Bigwood, R. Molecular Vibrational Energy Flow: Beyond the Golden Rule. *Int. Rev. Phys. Chem.* **1998**, *17*, 91–145.
- (120) Gruebele, M.; Wolynes, P. G. Vibrational Energy Flow and Chemical Reactions. *Acc. Chem. Res.* **2004**, *37*, 261–267.
- (121) Leitner, D. M.; Gruebele, M. Quantum Model of Restricted Vibrational Energy Flow on the Way to the Transition State in Unimolecular Reactions. *Mol. Phys.* **2008**, *106*, 433–442.
- (122) Miyasaka, H.; Ojima, S.; Mataga, N. Femtosecond–Picosecond Laser Photolysis Studies of the Ion-Pair Formation Process in the Excited State of the Charge-Transfer Complex in Solution. *J. Phys. Chem.* **1989**, *93*, 3380–3382.
- (123) Ojima, S.; Miyasaka, H.; Mataga, N. Femtosecond Picosecond Laser Photolysis Studies on the Dynamics of Excited Charge-Transfer Complexes in Solution. 1. Charge Separation Processes in the Course of the Relaxation from the Excited Franck–Condon State of 1,2,4,5-Tetracyanobenzene in Benzene and Methyl-Substituted Benzene Solutions. *J. Phys. Chem.* **1990**, *94*, 4147–4152.
- (124) Ojima, S.; Miyasaka, H.; Mataga, N. Femtosecond Picosecond Laser Photolysis Studies on the Dynamics of Excited Charge-Transfer Complexes in Solution. 2. Ion-Pair Formation Processes in the Excited-State of 1,2,4,5-Tetracyanobenzene Aromatic Hydrocarbon Complexes in Polar Solvents. *J. Phys. Chem.* **1990**, *94*, 5834–5839.
- (125) Ojima, S.; Miyasaka, H.; Mataga, N. Femtosecond Picosecond Laser Photolysis Studies on the Dynamics of Excited Charge-Transfer Complexes in Solution. 3. Dissociation into Free Ions and Charge Recombination Decay from the Ion-Pair State Formed by Charge Separation in the Excited-State of 1,2,4,5-Tetracyanobenzene Aromatic Hydrocarbon Complexes in Polar Solvents. *J. Phys. Chem.* **1990**, *94*, 7534–7539.
- (126) Larsen, D. S.; Ohta, K.; Fleming, G. R. Three Pulse Photon Echo Studies of Nondipolar Solvation: Comparison with a Viscoelastic Model. *J. Chem. Phys.* **1999**, *111*, 8970–8979.
- (127) Degradation of C153 was quickly observed for 383 nm excitation in chlorine-containing solvents. The data shown in Figure 10 were averaged for only about 5 min before noticeable changes due to degradation occurred.
- (128) Kovalenko, S. A.; Schanz, R.; Hennig, H.; Ernsting, N. P. Cooling Dynamics of an Optically Excited Molecular Probe in Solution from Femtosecond Broadband Transient Absorption Spectroscopy. *J. Chem. Phys.* **2001**, *115*, 3256–3273.
- (129) Zhou, J. W.; Shah, R. P.; Findley, B. R.; Braun, C. L. Long Distance Photoinduced Electron Transfer in Solutions: A Mechanism for Producing Large Yields of Free Ions by Electron Transfer Quenching. *J. Phys. Chem. A* **2002**, *106*, 12–20.
- (130) Gould, I. R.; Ege, D.; Moser, J. E.; Farid, S. Efficiencies of Photoinduced Electron-Transfer Reactions — Role of the Marcus Inverted Region in Return Electron Transfer within Geminate Radical-Ion Pairs. *J. Am. Chem. Soc.* **1990**, *112*, 4290–4301.
- (131) Gould, I. R.; Farid, S. Fluorescence of Excited Charge-Transfer Complexes and Absolute Dynamics of Radical-Ion Pairs in Acetonitrile. *J. Phys. Chem.* **1992**, *96*, 7635–7640.
- (132) Marcus, R. A. Free Energy of Nonequilibrium Polarization Systems. 2. Homogeneous and Electrode Systems. *J. Chem. Phys.* **1963**, *38*, 1858–1862.
- (133) Dogonadze, R. R.; Itskovitch, E. M.; Kuznetsov, A. M.; Vorotyntsev, M. A. Theory of Light Absorption by Ions in Solution. *J. Phys. Chem.* **1975**, *79*, 2827–2834.
- (134) Asahi, T.; Mataga, N. Charge Recombination Process of Ion-Pair State Produced by Excitation of Charge-Transfer Complex in Acetonitrile Solution — Essentially Different Character of Its Energy-Gap Dependence from That of Geminate Ion Pair Formed by Encounter between Fluorescer and Quencher. *J. Phys. Chem.* **1989**, *93*, 6575–6578.
- (135) Asahi, T.; Mataga, N. Femtosecond Picosecond Laser Photolysis Studies on the Dynamics of Excited Charge-Transfer Complexes — Aromatic Hydrocarbon–Acid Anhydride, Hydrocarbon–Tetracyanoethylene, and Hydrocarbon–Tetracyanoquinodimethane Systems in Acetonitrile Solutions. *J. Phys. Chem.* **1991**, *95*, 1956–1963.
- (136) Arnold, B. R.; Farid, S.; Goodman, J. L.; Gould, I. R. Absolute Energies of Interconverting Contact and Solvent-Separated Radical-Ion Pairs. *J. Am. Chem. Soc.* **1996**, *118*, 5482–5483.
- (137) Arnold, B. R.; Noukakis, D.; Farid, S.; Goodman, J. L.; Gould, I. R. Dynamics of Interconversion of Contact and Solvent-Separated Radical-Ion Pairs. *J. Am. Chem. Soc.* **1995**, *117*, 4399–4400.
- (138) Mohammed, O. F.; Vauthey, E. Simultaneous Generation of Different Types of Ion Pairs Upon Charge-Transfer Excitation of a Donor–Acceptor Complex Revealed by Ultrafast Transient Absorption Spectroscopy. *J. Phys. Chem. A* **2008**, *112*, 5804–5809.
- (139) Dedonder-Lardeux, C.; Gregoire, G.; Jouvet, C.; Martrenchard, S.; Solgadi, D. Charge Separation in Molecular Clusters: Dissolution of a Salt in a Salt–(Solvent)_n Cluster. *Chem. Rev.* **2000**, *100*, 4023–4038.
- (140) Petersen, C. P.; Gordon, M. S. Solvation of Sodium Chloride: An Effective Fragment Study of $\text{NaCl}(\text{H}_2\text{O})_n$. *J. Phys. Chem. A* **1999**, *103*, 4162–4166.
- (141) Mizoguchi, A.; Ohshima, Y.; Endo, Y. Microscopic Hydration of the Sodium Chloride Ion Pair. *J. Am. Chem. Soc.* **2003**, *125*, 1716–1717.
- (142) Onsager, L. Electric Moments of Molecules in Liquids. *J. Am. Chem. Soc.* **1936**, *58*, 1486–1493.
- (143) A B3LYP/6-31G(d) SCRF calculation with the polarizable continuum model (PCM) for BZ–TCNE in CH_2Cl_2 recommended a cavity radius of 0.492 nm.
- (144) The vibrational frequency and force constant of the D–A intermolecular stretch of the CT1 state calculated at the TD-M06HF/6-31G(d) level of theory is 194 cm^{-1} and $2.05 \times 10^{-8} \text{ N/nm}$, respectively.
- (145) Closs, G. L.; Miller, J. R. Intramolecular Long-Distance Electron-Transfer in Organic Molecules. *Science* **1988**, *240*, 440–447.
- (146) Barbara, P. F.; Meyer, T. J.; Ratner, M. A. Contemporary Issues in Electron Transfer Research. *J. Phys. Chem.* **1996**, *100*, 13148–13168.
- (147) Gould, I. R.; Farid, S.; Young, R. H. Relationship between Exciplex Fluorescence and Electron Transfer in Radical Ion Pairs. *J. Photochem. Photobiol. A* **1992**, *65*, 133–147.
- (148) Gould, I. R.; Noukakis, D.; Gomezjahn, L.; Young, R. H.; Goodman, J. L.; Farid, S. Radiative and Nonradiative Electron Transfer in Contact Radical-Ion Pairs. *Chem. Phys.* **1993**, *176*, 439–456.